1 **Impact of scale-aware deep convection on the cloud liquid and ice water paths and precipitation using the**

2 **Model for Prediction Across Scales (MPAS-v5.2)**

3 **Laura D. Fowler[1], Mary C. Barth[1], and Kiran Alapaty[2]**

4 [1]National Center for Atmospheric Research, Boulder, Colorado
5 [2]Center for Environmental Measurements and Modeling, U.S. Environmental Protection Agency
6 Research Triangle Park, North Carolina

8
9 September 2019
10
11
12
13
14
15
16
17
18
19
20
21
22
23
24
25
26
27
28
29
30
31
32
33
34
35
36
37
38
39
40
41
42
43
44
45
46
47
48

49 *Corresponding author address*: Dr. Laura D. Fowler, National Center for Atmospheric Research. P.O. Box 3000,

50 Boulder, CO 80307-3000, USA.

51 E-mail: laura@ucar.edu

Abstract. The cloud Liquid Water Path (LWP), Ice Water Path (IWP), and precipitation simulated with uniform- and variable-resolution numerical experiments using the Model for Prediction Across Scales (MPAS) are compared against Clouds and the Earth's Radiant Energy System (CERES) and Tropical Rainfall Measuring Mission data. Our comparison between monthly mean model diagnostics and satellite data focuses on the convective activity regions of the Tropical Pacific Ocean, extending from the Eastern Tropical Pacific Basin where trade wind boundary layer clouds develop to the Western Pacific warm pool defined by deep convective updrafts capped with extended upper-tropospheric ice clouds. Using the scale-aware Grell-Freitas (GF) and Multi-Scale Kain-Fritsch (MSKF) convection schemes with the Thompson cloud microphysics scheme, uniform-resolution experiments produce large biases between simulated and satellite-retrieved LWP, IWP, and precipitation. Differences in the treatment of shallow convection lead the LWP to be strongly overestimated when using GF while being in relatively good agreement when using MSKF compared to CERES data. Over areas of deep convection, numerical experiments using MSKF lead to increased IWP than those using GF, in conjunction with increased convective detrainment of cloud ice and ice nucleation. Mesh refinement over the Western Pacific warm pool yields increased grid-scale condensation, LWP, IWP, and cloudiness over the refined area of the mesh associated with increased grid-scale upward vertical motions. Results underscore the importance of evaluating clouds, their optical properties, and the top-of-the-atmosphere radiation budget in addition to precipitation when performing mesh refinement global simulations.

1 Introduction

Comparing simulated against observed global cloud liquid and ice water paths (LWP and IWP) remains challenging because of uncertainties in parameterizing moist processes and cloudiness in global climate and numerical weather prediction (NWP) models, and errors in retrieving the LWP and IWP from satellite measurements. Cloud simulations from general circulation models (GCMs) involved in Phase 3 and 5 of the Coupled Model Intercomparison Project (CMIP3; CMIP5; Meehl et al, 2007; Taylor et al., 2012) display a strong disparity in the simulated LWP (Jiang et al., 2012; Li et al., 2018) and IWP (Li et al., 2012), producing annual mean LWP and IWP overestimated by factors of 2 to 10 when compared to satellite data. Satellite observations of the LWP and IWP from passive nadir viewing instruments such as the Moderate-resolution Imaging Spectroradiometer (MODIS; Minnis et al., 2011), and profiling radar such as the 94-GHz instrument on the CloudSat satellite (Stephens et al., 2002), also display major differences among themselves, as discussed in Li et al. (2008) and Waliser et al. (2009). While models and satellite retrievals agree that the LWP and IWP should be defined as the vertically-integrated liquid and ice water content, including all nonprecipitating and precipitating hydrometeors, this is not always the case in practice, further challenging a clearly-posed data-data and model-data comparison. Defining the LWP and IWP varies between models, depending on the complexity of the parameterization of cloud microphysics processes and prognostic versus diagnostic treatment of falling hydrometeors. Defining the measured LWP and IWP varies between satellite products, depending on the sensitivity of the observing systems to detect large precipitating particles. While comparing simulated and observed LWP and IWP may not be as straightforward as comparing the top-of-the-atmosphere (TOA) radiation budget (Dolinar et al., 2015; Stanfield et al., 2015), it offers a different way to directly diagnose biases in simulated total cloud liquid

87   and ice water mass as a first step to help correct deficiencies in parameterizing global scale moist processes and

88   precipitation.

89   Before the launch of the CloudSat and Cloud-Aerosol Lidar and Infrared Pathfinder Satellite Observation mission

90   (Stephens et al., 2002), global estimates of the LWP and IWP were retrieved principally from satellite radiance

91   measurements over different spectral intervals (e.g., Alishouse et al., 1990; Greenwald et al., 1993; Minnis et al., 1995;

92   Platnick et al., 2003). In their critical review of most common methods developed to retrieve cloud and precipitation

93   properties from satellite radiances, Stephens and Kummerow (2007) identify two main sources of errors. The first

94   source of errors originates from the mandatory classification between cloudy and cloud-free scenes, and between

95   precipitating and non-precipitating cloudy scenes. The second source of errors stems from using forward radiative

96   transfer models that lack details of the vertical distribution of cloudiness and precipitation as well as complexity in

97   specifying the optical properties of liquid water and ice particles. Estimating the LWP and IWP from CloudSat radar

98   reflectivities alone presents its own set of challenges for scenes that include precipitating cloud systems due to the

99   high sensitivity of radar reflectivities to the presence of large particles, for scenes that include mixed-phase and deep

100   convective clouds, and close to the surface due to ground clutter. Li et al. (2018) show that annual mean maps of

101   MODIS- and CloudSat-based LWP agree relatively well in tropical and subtropical regions if both data sets exclude

102   LWP observations for deep convective/precipitating clouds since MODIS is quite insensitive to precipitation.

103   Stephens and Kummerow (2007) advocate combining satellite-retrieved radar and radiance measurements to help

104   validate simulated cloud properties and precipitation. In addition to considering the impact of precipitating particles,

105   Waliser et al. (2009) demonstrate that a well-posed model-data comparison must include a consistent sampling

106   between model outputs and satellite data to reduce diurnal sampling biases and sensitivity of the sensor and retrieval

107   algorithm to the particle size when computing the simulated LWP and IWP.

108   Contemporary climate and NWP GCMs (Giorgetta et al., 2018; Molod et al., 2012; Kay et al., 2015, Skamarock

109   et al., 2012) categorize moist processes into three distinct parameterizations, one to simulate turbulent mixing in the

110   Planetary Boundary Layer (PBL) in response to surface forcing and forcing in the free troposphere, one to simulate

111   subgrid scale shallow and deep convection, and one to include grid-scale cloud microphysics. While coupling between

112   parameterizations varies between GCMs, it is an established practice to let detrained condensates from convective

113   updrafts serve as sources for non-convective grid-scale clouds, as precipitating anvils and cirrus outflow. We suggest

114   that uncertainties in parameterizing moist convection and impact on grid-scale clouds may explain a major part of the

115   differences in the LWP and IWP simulated between the CMIP3 and CMIP5 GCMs. In recent years, efforts have been

116   made to develop unified cloud parameterizations to represent all cloud types and alleviate the need to parameterize

117   complex interactions between stratiform, shallow convective, and deep convective clouds (Guo et al., 2015; Storer et

118   al., 2015; Thayer et al., 2015). Using the global Model for Prediction Across Scales (MPAS; Skamarock et al., 2012),

119   Fowler et al. (2016) discuss the sensitivity of simulated precipitation as spatial resolution increases from hydrostatic

120   to nonhydrostatic scales and suggest to further analyze the associated sensitivity of simulated clouds and TOA

121   radiation. Results show that as subgrid scale convective motions are increasingly resolved, diagnostic precipitation

122   from the scale-aware Grell-Freitas (GF; Grell and Freitas, 2014) deep convection scheme decreases while prognostic

123   precipitation from the WSM6 (Hong and Lim, 2006) cloud microphysics scheme increases over the refined area of

124   the variable-resolution mesh. Vertical profiles of the cloud liquid and ice water mixing ratios and cloud fraction

125   highlight the redistribution of cloud condensates and relative humidity with height in the refined area in response to

126   decreased contribution of convective detrainment of cloud liquid water and ice. However, Fowler et al. (2016) do not

127   further address if variations in the vertical profiles of cloud condensates lead to improved LWP, IWP, and cloud optical

128   properties against satellite-derived data.

129   The objectives of our research are threefold. First, we want to assert that our suite of PBL, deep and shallow

130   convection, and cloud microphysics parameterizations tested in MPAS at hydrostatic and nonhydrostatic scales for

131   medium-range spring forecasts over the Continental United States (Schwartz, 2019; Wong and Skamarock, 2016) can

132   also be used to produce month-long simulations of tropical convection, narrowing our analysis on the Tropical Pacific

133   Ocean. In order to broaden our research and possibly generalize our results, we implemented the scale-aware

134   MultiScale Kain-Fritsch (MSKF; Glotfelty et al., 2019; Zheng et al., 2016) parameterization of deep and shallow

135   convection in addition to GF. Second, we want to evaluate the ability of MPAS to simulate the LWP, IWP, cloudiness,

136   and TOA long- and short-wave radiation against the Clouds and the Earth's Radiant Energy System (CERES; Wielicki

137   et al., 1996) Single Scanner FootPrint (SSF; Minnis et al., 2011) data set, and precipitation against the TRMM

138   Multisatellite Precipitation Analysis (TMPA; Huffman et al., 2007). Our third goal aims at understanding differences

139   in the LWP, IWP, precipitation, and cloud radiative effects as functions of horizontal resolution with GF and MSKF

140   using the capability of local mesh refinement developed for MPAS.

141   In Section 2, we summarize the characteristics of the GF and MSKF parameterizations of deep and shallow

142   convection. In Section 3, we provide a short description of MPAS, including physics parameterizations used with both

143   convective parameterizations, the design of our experiments with uniform- and variable-resolution meshes, and

144   description of the satellite data sets used to validate our results. In Section 4, we analyze our results in terms of

145   precipitation and varying contribution of the convective and grid-scale precipitation to the total precipitation as a

146   function of spatial resolution. In Section 5, we compare the LWP, IWP, and TOA long- and short-wave radiation

147   against satellite data. In Section 6, we summarize our results and propose areas of future research.

2   Description of the convective parameterizations0

149   Mass flux-based convective parameterizations distinguish themselves through the use of different triggering functions

150   to initiate convection, the details of their entraining-detraining cloud models, and formulation of their closures that

151   control the intensity of convection and computation of the cloud base mass flux. For convective parameterizations that

152   include deep and shallow convection, criteria that characterize the two kinds of convection strongly vary. Furthermore,

153   how convective parameterizations account for the dependence of convection on the horizontal resolution differs in

154   complexity. In this section, we summarize the chief characteristics of GF and MSKF, including differences in their

155   treatment of deep and shallow convection, and spatial-scale dependence.

2.1   The Grell-Freitas (GF) parameterization

157   The version of GF used in our numerical experiments is that implemented in version 3.8.1 of the Advanced Research

158   Weather Research Forecast model (Skamarock et al., 2008), as described in Grell and Freitas (2014). Its properties

159   were first discussed in Grell (1993) and later expanded by Grell and Devenyi (2002) to include stochasticism. GF

160   treats deep and shallow convection separately by using different initial entrainment rates ($7\text{x}10^{-5}$ m^{-1} and $1\text{x}10^{-2}$ m^{-1}

161   for deep and shallow convection, respectively) to control the depth of convective cloud layers and closures to calculate

162   the cloud base mass flux. GF includes an ensemble of closures from well-known convective parameterizations to

163   compute a mean cloud-base mass flux. For deep convection, these four closures are the *AS* closure (Arakawa and

164   Schubert, 1974) that assumes instantaneous equilibrium between the large-scale forcing and subgrid-scale convection;

165   the *W* closure (Brown, 1979; Frank and Cohen, 1987) that relates the cloud base mass flux to the grid-scale upward

166   vertical velocity; the *MC* closure (Krishnamurti et al., 1983) that calculates the cloud base mass flux as a function of

167   the vertically-integrated vertical moisture advection; and the *KF* closure (Kain and Fritsch, 1993) that reduces the

168   convective available potential energy over a prescribed convective time-scale. Qiao and Liang (2015) analyze the

169   separate and combined impacts of the four closures on the simulated summer precipitation over the United States

170   coastal oceans. On the one hand, they found that computing the cloud base mass flux using the *W* and *MC* closures

171   led to precipitation patterns and amounts that are in better agreement against TMPA data than those using the *AS* and

172   *KF* closures. On the other hand, they found that the *AS* and *KF* closures yield improved diurnal cycle of precipitation

173   relative to the other two closures. In our numerical experiments, GF gives an equal weight to each closure to calculate

174   the mean cloud base mass flux for deep convection. As for deep convection, GF includes different closures for shallow

175   convection. In our numerical experiments using GF, we choose the boundary layer quasi-equilibrium (*BLQE*) closure

176   of Raymond (1995) for shallow convection.

177   Both types of convection transport total water and moist static energy in a conservative manner but neglect to

178   include ice phase processes in updrafts and downdrafts. In this version of GF, the only feedback between shallow

179   convection and the large-scale environment is lateral and cloud-top detrainment of water vapor and corresponding

180   heating, as liquid water formed in shallow updrafts evaporates immediately. Deep convection returns potential

181   temperature, water vapor, and condensed water tendencies to the environment. Detrained condensed water acts as a

182   source of liquid water (ice) if the large-scale temperature is warmer (colder) than the prescribed 258 K threshold.

183   While GF assumes that shallow convective plumes are not deep enough to produce precipitation, the conversion of

184   liquid water to rain water in deep convective plumes depends on a simple Kessler-type (Kessler, 1969) conversion

185   threshold and precipitation reaches the surface instantaneously.

186   As discussed in Grell and Freitas (2014), deep convection includes a simplified representation of the unified

187   parameterization of deep convection described in Arakawa and Wu (2013). Arakawa and Wu (2013) demonstrate that

188   mass flux-based convective parameterizations can be modified to work at all resolutions spanning between hydrostatic

189   and non-hydrostatic scales through the reduction of the convective vertical eddy transport as a quadratic function of

190   the horizontal fraction of the grid box occupied by convective updrafts. In GF, the convective updraft fraction (σ) is

191   computed as a simple function of the initial entrainment rate ($\varepsilon = 7\text{x}10^{-5}$ m^{-1}) and half-width radius (R) of convective

192   updrafts following Simpson and Wiggert (1969), or

193
$$\sigma = \frac{\pi R^2}{A} \quad \text{and} \quad R = \frac{0.2}{\varepsilon} \tag{1}$$

194   where A is the area of the grid box. In Eq. (1), σ cannot exceed 0.7, as discussed in Fowler et al. (2016). Figure 1.a

195   highlights the rapid decrease in σ from 0.7 to 0.3 as spatial resolutions decrease from 6.1 to 9.2 km. σ further decreases

196   from 0.3 to 0.1 for resolutions between 9.2 and 16 km, and from 0.1 to 0.05 for resolutions spanning between 16 and

197   30 km. The $(1-\sigma)^2$ quadratic function used to scale the cloud-base mass flux starts to significantly impact the cloud-

198   base mass flux at resolutions greater than 20 km. Using a variable-resolution mesh varying between 50 km over the

199   coarse area of the mesh down to 3 km over the refined area of the mesh centered over South America, Fowler et al.

200   (2016) show that the impact of parameterized convection weakens and that of grid-scale vertical motion strengthens

201   as horizontal grid-spacing increases from hydrostatic to non-hydrostatic scales.
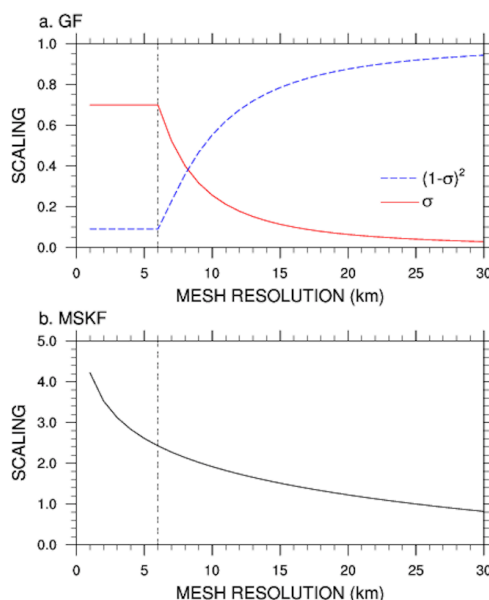
202
203   **Figure 1:** a) Convective updraft fraction as a function of the mesh resolution used to scale the cloud base mass flux in GF; and b)
204   Scaling factor as a function of the mesh resolution used to scale the convective time scale in MSKF.

205   **2.2   The Multi-Scale Kain-Fritsch (MSKF) parameterization**

206   MSKF is the scale-aware version of the Kain-Fritsch (KF) convective parameterization, first developed by Kain and

207   Fritsch (1990; 1993), and later updated by Kain (2004) to include, among other improvements, non-precipitating

208   shallow convection. The trigger function is that used in Fritsch and Chappell (1980), originally tested in Kain and

209   Fritsch (1992) and recently in Suhas and Zhang (2014). In MSKF, convection may be triggered if the temperature of

210   a *mixed layer* is greater than that of the environment. The pressure thickness of the mixed layer is the sum of adjacent

211   layer depths until it reaches at least 50 hPa starting at the layer next to the surface. The mixed layer temperature is a

212   pressure-weighted function of the temperatures in those adjacent layers after being lifted to the Lifting Condensation

213   Level (LCL) plus a perturbation temperature linked to the magnitude of the grid-scale vertical motion at the LCL.

214   Once the base of a potential updraft source layer is found, convection remains activated if the vertical velocity of an

215   air parcel lifted using the Lagrangian parcel method remains positive for a minimum cloud depth of 3 km, as a test

216   that the convective instability is strong enough for the air parcel to reach the Level of Free Convection (LFC). If not,

217   the procedure is repeated by moving up to the next model layer until a new updraft source layer is found or until the

218   search reaches above the lowest 300 hPa of the atmosphere. Further details on the equations used to compute the

219   perturbation temperature and parcel vertical velocity are found in Kain (2004).

220   In MSKF, the closure assumption assumes that the Convective Available Potential Energy in a cloud layer is

221   removed within a time adjustment period following Bechtold et al. (2001). The convective time scale is defined as the

222   advective time scale in the cloud layer with maximum values of 1 h and 0.5 h for deep and shallow convection,

223   respectively. In contrast to GF, the thermodynamics inside the cloud model includes the ice phase. The condensed

224   water formed in each cloudy layer is partitioned between liquid water and ice, assuming a linear transition of the cloud

225   temperature between 268 K and 248 K. A fraction of the condensed water converts to rain, following Ogura and Cho

226   (1973), and reaches the ground instantaneously. As discussed in Kain (2004), when an updraft source layer is

227   identified, the classification of a convective cloud layer as deep or shallow depends on the cloud depth. Shallow

228   convection is activated when all the criteria for deep convection are met, but the depth of the updraft is shallower than

229   the minimum cloud depth (3 km). This definition implies that shallow and deep convection are not allowed to coexist.

230   In the case of shallow convection, precipitation formed in updrafts is detrained to the environment as rain or snow,

231   providing an additional moisture source to the large-scale environment. As in GF, MSKF provides tendencies of

232   temperature, water vapor, cloud liquid water/ice to the environment, and tendencies of rain and snow from shallow

233   convection.

234   MSKF contains many improvements over KF, as summarized in the supplemental material of Glotfelty et al.

235   (2019). These improvements include subgrid-scale cloud feedbacks to radiation from both shallow and deep

236   convection leading to more realistic surface downward radiation, as described in Alapaty et al. (2012), and the scale

237   dependence of fundamental parameters so that MSKF can be used at spatial resolutions varying between hydrostatic

238   and nonhydrostatic scales. As detailed in Glotfelty et al. (2019) and Zheng et al. (2016), MSKF uses a scale dependent

239   formulation (β) to the adjustment time scale (τ) for deep and shallow convection based on Bechtold et al. (2008), or

240
$$\boldsymbol{\tau = \frac{H}{W_{cl}}\, \beta} \quad \text{and} \quad \boldsymbol{\beta = 1 + ln\left(\frac{25}{\Delta x}\right)} \qquad (2)$$

241   where H and W_{cl} are the depth of the convective cloud and cloud-averaged vertical velocity scale, and Δx is the grid

242   spacing. Figure 1.b highlights the dependence of the β scaling parameter as a function of horizontal resolution. As

243   many MSKF parameters are optimized for a resolution around 25 km (Kain, 2004), β is equal to 1 at 25 km, ramping

244   up to values greater than 2.4 for resolutions higher than 6km. Because the adjustment time scale is proportional to

245   β (Zheng et al., 2016), it increases as horizontal resolution increases, leading to scale-aware stabilization of the

246   atmosphere by MSKF. In addition, MSKF includes a new scale-aware formulation of the minimum entrainment rate

247   using the LCL as a function of the scale-dependent *Tokioka* parameter (Tokioka et al., 1988), a scale-dependent

248   conversion rate for liquid water and ice condensates to precipitation, an increased grid-scale velocity expressed in

249   terms of the subgrid scale updraft mass flux, and elimination of double counting of precipitation in cloudy layers. The

250   separate and combined impacts of the development of MSKF on high resolution weather forecasts and regional climate

251   simulations are discussed in Herwehe et al. (2014), Mahoney (2016), He and Alapaty (2018), Zheng et al. (2016), and

252   Glotfelty et al. (2019).

3 Methodology

3.1 Numerical experiments

We discuss differences in our MPAS results between GF and MSKF configurations on precipitation, cloud properties, and TOA radiation using 30-day long numerical experiments in MPAS (Skamarock et al., 2012). MPAS is a global nonhydrostatic atmospheric model developed for NWP and climate studies. The horizontal discretization uses an unstructured spherical centroidal Voronoi tessellation with a C-grid staggering, as described in Ju et al. (2011), while the vertical discretization is the height-based hybrid terrain-following coordinate of Klemp (2011). The dynamical solver integrates the prognostic equations (cast in flux form) for the horizontal momentum, vertical velocity, potential temperature, dry air density, and scalars using the split-explicit technique of Klemp et al. (2007). The temporal discretization uses a third-order Runge-Kutta scheme and the explicit time-splitting technique described in Wicker and Skamarock (2002). We use the monotonic option of the scalar transport scheme of Skamarock and Gassmann (2011) for horizontal and vertical advection of all moist scalars on the unstructured Voronoi mesh. Finally, horizontal filtering of the state variables is based on Smagorinsky (1963) in which the horizontal length scale is defined as the minimum distance between cell centers.

In MPAS, the computational flow includes three distinct steps. The first step calls the physics parameterizations that update the surface energy budget and calculate the tendencies of potential temperature, moist species, and zonal and meridional wind due to long- and short-wave radiation, sub-grid scale convection, condensation and mixing in the PBL and free troposphere, and gravity wave drag due to orography. The physics parameterizations use the same input surface boundary conditions and soundings to compute their respective tendencies. Besides GF and MSKF, these parameterizations are,

- the Noah land surface parameterization described by Chen and Dudhia (2001),
- the long- and short-wave Rapid Radiative Transfer Model for GCMs (RRTMG) described by Mlawer et al. (1997) and Iacono et al. (2000),
- the semi-empirical parameterization of the cloud fraction of grid-scale clouds from Xu and Randall (1996) and convective clouds from Xu and Krueger (1991) for use in the long- and short-wave RRTMG schemes. Following Xu and Randall (1996), the fractional amount of grid-scale clouds is a function of the relative humidity and grid-averaged condensate mixing ratio of cloud liquid water, ice, and snow. In MSKF, the fractional amount of shallow and deep convective clouds depends on the convective mass flux.
- the Mellor–Yamada–Nakanishi–Niino (MYNN) Planetary Boundary Layer (PBL) and surface layer scheme described by Nakanishi and Niino (2009) with many updates described in Olson et al. (2019), and
- the gravity wave-drag parameterization of Hong et al. (2008).

The second step calls the dynamical solver which updates the state variables with their respective diabatic tendencies in conjunction to applying horizontal and vertical advection. Finally, the third step calls the grid-scale cloud microphysics parameterization so that at the end of the model time step, supersaturation has been entirely removed or the relative humidity does not exceed 100%. Unlike the physics parameterizations listed for step one, the grid-scale cloud microphysics scheme updates the potential temperature and moist species for the next time step instead of

289   providing individual tendencies. The bulk cloud microphysics parameterization of Thompson et al. (THOM; 2004,
290   2008) is used in all our numerical experiments. THOM includes prognostic equations for temperature, mass mixing
291   ratio of water vapor, cloud liquid water, rain, cloud ice, snow, and graupel, and number concentration of cloud ice and
292   rain. We set the number concentration of cloud droplets to 300×10^6 m^{-3} over land and 100×10^6 m^{-3} over oceans. In
293   RRTMG, we diagnose the radiative effective radii of cloud liquid water, cloud ice, and snow as functions of the
294   THOM cloud particle assumptions to add coupling between the cloud microphysics and cloud optical properties, as
295   discussed in Thompson et al. (2016).

296   To compare the two convective parameterizations against satellite-derived data at hydrostatic scales, we use a
297   quasi-uniform resolution mesh for which the mean distance between cell centers is 30 km, corresponding to 655,362
298   cells. The vertical scale includes 55 layers with monotonically increasing thicknesses varying from 50 meters next to
299   the surface to 700 meters below 10 km to 1000 meters below the model top over ocean cells. The model top is set at
300   30 km. The dynamics and physics time steps are both set to 150 s, and the horizontal diffusion length scale is set to
301   30 km. Long- and short-wave radiation is called every 15 mins and THOM is cycled twice so that the cloud
302   microphysics time-step is less than 90 s to ensure computational stability (Thompson, private communication). With
303   each convection scheme, we have performed a one-month long experiment preceded by a two-day spin-up to simulate
304   Northern Hemisphere early winter, initializing our experiments with ERA-Interim (Dee et al., 2011) reanalyses for
305   0000 UTC 29 November 2015. ERA-Interim sea surface temperatures and sea ice fractions are used to update ocean
306   cells daily. We refer to our quasi-uniform resolution experiments run with GF and MSKF as GFu and MSKFu,
307   respectively.

308   **3.2   Sensitivity experiments**

309   Using a variable-resolution mesh spanning between 50 km and 3 km in MPAS, Fowler et al. (2016) demonstrate that
310   subgrid-scale convection parameterized with GF weakens and grid-scale cloud microphysics parameterized with
311   WSM6 (Hong and Lim, 2006) strengthens as resolution increases from the coarse to most refined area of the mesh.
312   Over the most refined area, grid-scale precipitation contributes a major part to total precipitation, and vertical profiles
313   of subgrid -scale convective heating and drying resemble those obtained with a precipitating shallow convection
314   scheme. Fowler et al. (2016) later suggest investigating the effect of variable resolution on cloud macrophysical
315   properties and TOA radiation, as condensation and precipitation shift from being parameterized rather simply in the
316   GF convective cloud model to being described in detail in WSM6. With the aim to quantify changes in cloud properties
317   and radiation across scales using GF and MSKF, we repeat the early winter experiments but with a variable-resolution
318   mesh that spans between 30 km and 6 km and includes 1,622,018 cells. As shown in Fig. 2.a, we centered the refined
319   area of the mesh over the Pacific warm pool which we defined as the area in the Western Pacific Ocean where sea-
320   surface temperatures (SSTs) exceed 28.5°C, or between 170°E and 140°W. East of 140°W, the north-south width of
321   warmest SSTs across the transition zone between the refined and coarse mesh narrows to delineate the location of the
322   ITCZ in the Tropical Eastern Pacific. West of 170°E, the end of mesh refinement borders the eastern tip of Papua New
323   Guinea. Along the Equator, the transition zone between nonhydrostatic and hydrostatic scales spans 20° in the
324   meridional direction on either side of the most refined area of the mesh. Figure 2.b displays a histogram of the mean
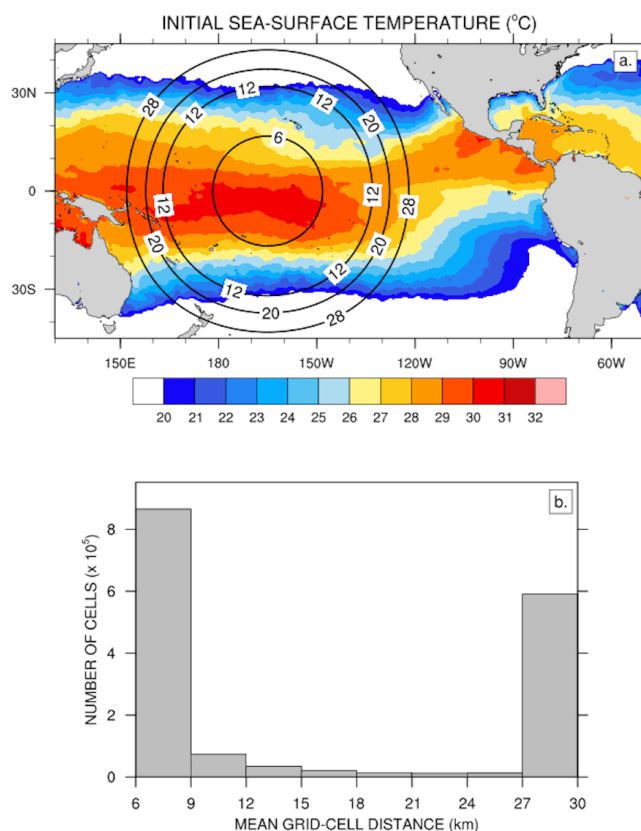
325
326 **Figure 2:** a) Initial sea-surface temperature and refined variable-resolution mesh depicted using isolines of the mean distance
327 between grid-cell centers (km) over the Tropical Pacific Ocean; and b) histogram of the number of cells as a function of the mean
328 distance between grid-cell centers.

329 distance between cell centers. Differences between the initialization of the variable- versus quasi uniform-resolution

330 experiments include a reduced time-step from 150 s to 30 s and a reduced horizontal diffusion length scale from 30

331 km to 6 km. Also, THOM is called only once per time-step. We refer to our variable-resolution experiments run with

332 GF and MSKF as GFv and MSKFv, respectively. Differences between GFu, GFv, MSKFu, and MSKFv are listed in

333 Table 1.

334

	GFu	MSKFu	GFv	MSKFv
No. of cells	655,362	655,362	1,622,018	1,622,018
Min. cell distance (km)	22.8	22.8	4.4	4.4
Max. cell distance (km)	31.8	31.8	37.8	37.8
Time step (s)	150	150	30	30
Diffusion length scale (km)	30	30	6	6
CP	GF	MSKF	GF	MSKF

335 **Table 1:** Horizontal mesh resolution, minimum and maximum distance between grid-cell centers, time-step, horizontal diffusion
336 length scale, and convective parameterization (CP) for numerical experiments with the quasi uniform- and variable-resolution
337 meshes.

338 **3.3   Satellite data sets**

339 We compare the cloud liquid water path (LWP) and ice water path (IWP), cloud area fraction (CF), and the top-of-
340 the-atmosphere longwave upward (TOALW) and shortwave net (TOASW) radiation simulated in our numerical
341 experiments against the Edition-4 Single Scanner Footprint (SSF) products from the Clouds and the Earth's Radiant
342 Energy System (CERES; Wielicki et al., 1996). Minnis et al. (2011) describe in great details the retrieval of
343 simultaneous and collocated radiation fluxes and cloud properties from the CERES radiometers and the Moderate-
344 resolution Imaging Spectroradiometer (MODIS) using consistent algorithms and calibration across satellite platforms,
345 and shared auxiliary input (temperature and humidity profiles). SSF data are available in two different formats. The
346 first data file format contains one hour of radiation fluxes and cloud properties at the instantaneous CERES 20 km
347 footprint level from the sun-synchronous afternoon (morning) equatorial crossing time Aqua (Terra) satellites. As
348 illustrated in Minnis et al. (2011; their Fig. 15), the CF in each SSF is given in terms of a clear fraction, a fraction for
349 an upper and lower cloud layer separately, and a fraction for an upper layer over a lower layer, although the overlap
350 CF is not available and set to zero in the Edition 4 release version that we are using. The LWP, IWP, and all other
351 cloud fields are provided for the lower and upper layers, separately. Figure 3 illustrates two orbits of the Aqua satellite,
352 one between 00 GMT and 01 GMT, and one between 14 GMT and 15 GMT, showing the TOALW (top panel) and
353 CF (bottom panel), after gridding the hourly orbital data to a 0.2°x0.2° latitude-longitude grid. Gridded radiation fluxes
354 and cloud data are means over all SSF data contained inside each rectangular grid, after applying a linear interpolation
355 to reduce the number of missing values. Missing values, highlighted in gray in all figures, depict rectangular grids that
356 did not contain radiation and cloud data in any of the SSF inside the 0.2°x0.2° grid. As seen in Fig. 3, our gridding of
357 the orbital data removes most of the missing data along each orbit, providing a clear depiction of the relationship
358 between the TOALW and CF for cloudy and cloud-free grid cells. Areas of high (low) TOALW coincide with areas
359 of small (large) cloudy areas, but it is also interesting to note that areas of each orbit are characterized as overcast in
360 conjunction with areas that are not as spatially uniform in TOALW as in CF.
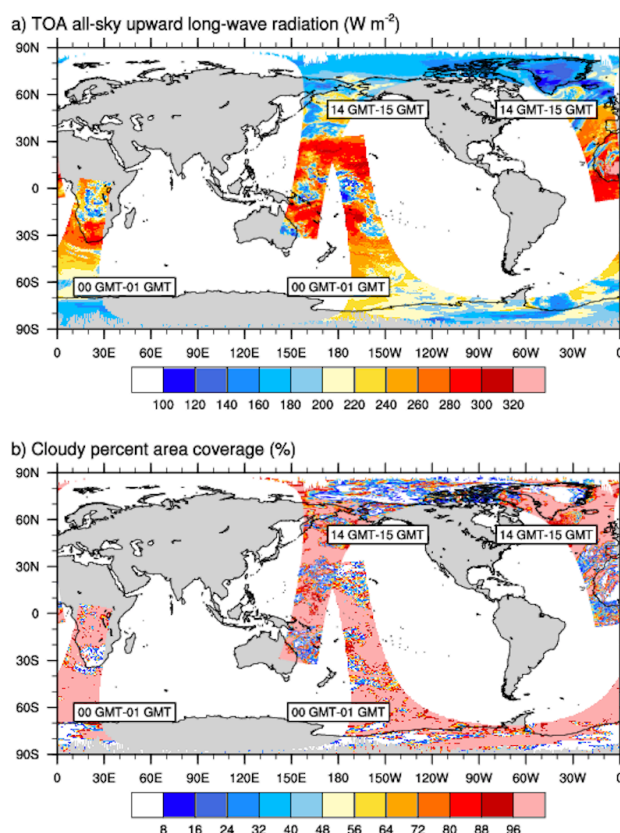
Figure 3: Orbital paths of the Aqua satellite between 00 GMT-01 GMT and 14 GMT-15 GMT after binning the SSF data onto a 0.2°x0.2° rectangular grid for a) the TOA all-sky upward long-wave radiation, and b) the cloudy percent area coverage for 1st December 2015.

The second data file format (SSF1deg) includes daily and monthly averages of the original SSF orbital data but interpolated on a 1°x1° latitude-longitude grid. The difficulty in using hourly higher-resolution orbital data instead of monthly mean lower-resolution 1°x1° latitude-longitude gridded product is that the former are available in two distinct *dynamic* layers while the latter is provided at fixed pressure levels and for the atmospheric column. The lower and upper layers are referred to as *dynamic* layers because the cloud-top (base) pressure of each layer varies between SSFs along each orbit. The advantage of using orbital hourly data is that they can be gridded and interpolated to a spatial resolution close to that of our uniform and variable-resolution numerical experiments prior to computing monthly mean radiation and cloud fields. We choose the 0.2°x0.2° latitude-longitude gridded hourly data derived from the first data file format through the entire manuscript.

In order to best compare the simulated against satellite-derived LWP and IWP, we need to understand the partitioning of the SSF LWP and IWP between the two cloud layers. In brief, a lower and an upper cloud layer can be detected simultaneously if they lie adjacent to each other inside an SSF. In that case, the cloud properties for each layer are reported separately. In the case when an opaque upper cloud layer is detected to be above a lower cloud layer, it is impossible to identify the two layers separately. Then, only one cloud layer is reported and always classified

379 as the lower cloud layer, regardless of its cloud-base (top) pressure (Loeb, private communication). Further details on

380 the cloud classification, including determination of the cloud phase, are found in Geier et al. (2003) and Minnis et al.

381 (2011). Figure 4 shows the monthly-mean LWP, IWP, and CF for the lower (left panels) and upper (right panels) layer

382 measured by Aqua for December 2015 over the Tropical Pacific Ocean. Figure S1 is as Fig. 4, but for the Terra satellite

383 (see supplemental figures). LWP and IWP are *in-cloud* values meaning that they have not been weighted by CF. The

384 lower cloud layer includes stratiform clouds that form over colder sea-surface temperatures along the coast of Peru

385 and off the Baja Peninsula. Over these areas of CF greater than 72% for the lower cloudy layer, CF for the upper cloud

386 layer is less than 8%, highlighting that a single layer of low-level clouds fills a major fraction of the SSF. Increased

387 values of CF are seen in conjunction with increased (decreased) values for the LWP (IWP) in the lower cloud layer

388 indicative of warm-phase clouds, as well seen as off the coast of Peru. High values for the CF and IWP juxtaposed

389 with lower values for the LWP in the lower cloud layer depict clearly deep convection over the Eastern Pacific Ocean,

390 ITCZ, and warm pool region. Over areas of deep convection, upper cloud layers are often detected in conjunction with

391 lower cloud layers within the same SSF but are defined by decreased values for the CF and IWP. For the LWP, the

392 coexistence of a lower and upper cloud layer is quite infrequent, as seen by the number of missing grid-points in Fig.

393 4.b (S1.b). Where detected, the LWP in the upper layer exceeds that in the lower layer, indicative of warm-phase

394 mature thicker cumulus clouds coexisting with developing thinner cumulus clouds in the lower layer. Finally, outside

395 of the typical stratus cloud regions and either sides of the ITCZ and warm pool region, SSF data reveal extended

396 regions of warm-phase thinner clouds characteristic of widespread shallow convection over tropical oceans.
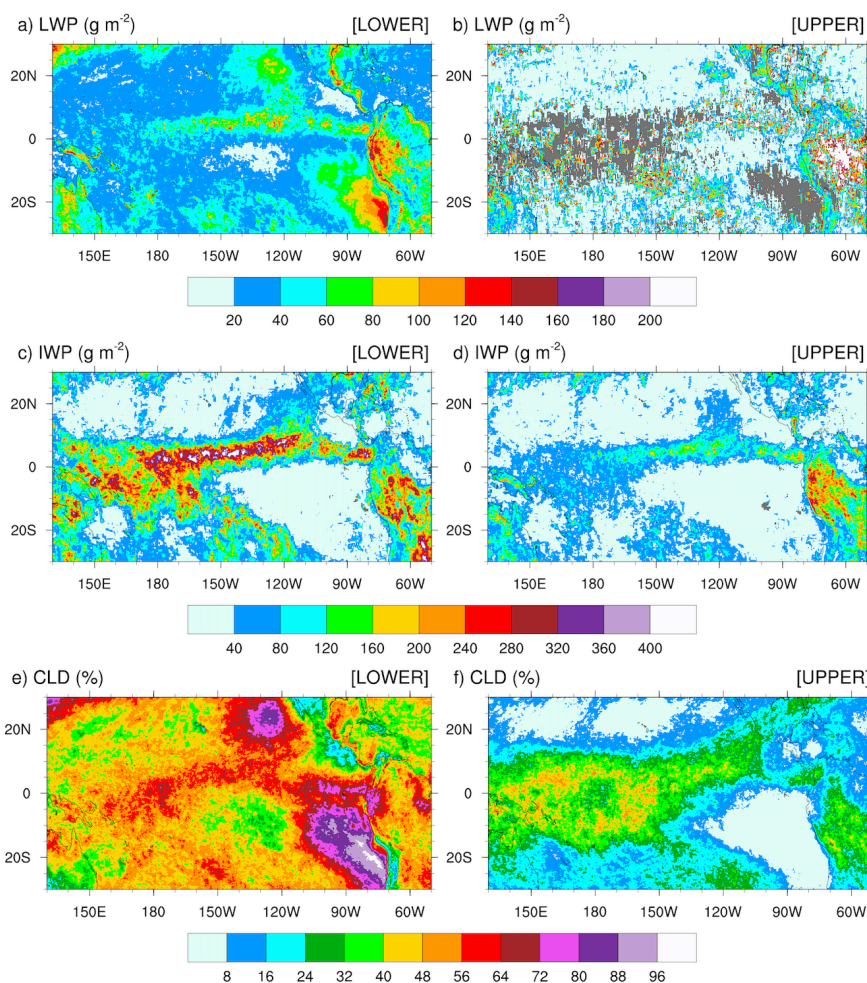
Figure 4: Monthly-mean cloud liquid water path (LWP, top panels), cloud ice water path (IWP, middle panels), and cloud fraction (CLD, bottom panels) over the Tropical Pacific Ocean for December 2015 from the Aqua satellite. Panels a), c), and e) are for the lower cloud layer; panels b), d), and f) are for the upper cloud layer.

Calculating the satellite-retrieved LWP and IWP in an atmospheric column for validation of those from our numerical simulations is a two-step process. Because simulated LWPs and IWPs are *gridcell mean* values and not *local* values, we first multiply the SSF LWP and IWP by CF to get their mean values in the lower and upper cloud layers separately, prior to gridding the hourly orbital data. Second, because the lower and upper layers are defined as adjacent to each other and never overlap in a SSF, we simply add the gridcell mean LWP and IWP in the lower layer to that in the upper layer to compute the total LWP and IWP. Our processing method is simpler than the processing steps taken by the CERES Science Team to spatially grid and temporally average SSF hourly orbital data to SSF1deg gridded monthly mean data. Figure 5 compares the monthly-mean 0.2°x0.2° latitude-longitude CF-weighted LWP and IWP and CF (left panels) against the SSF1deg products (right panels) for December 2015 over the Tropical Pacific Ocean. The top panels of Fig. 5 show that our method reproduces successfully the geographical patterns and magnitude

411   of the LWP over the Tropical Pacific when compared against the SSF1deg data for both months. In contrast, because

412   our method does not weigh the IWP as a function of height, it systematically overestimates the SSF IWP when

413   compared against the SSF1deg data, as seen over the ITCZ and South Pacific Convergence Zone (SPCZ) in both

414   months.
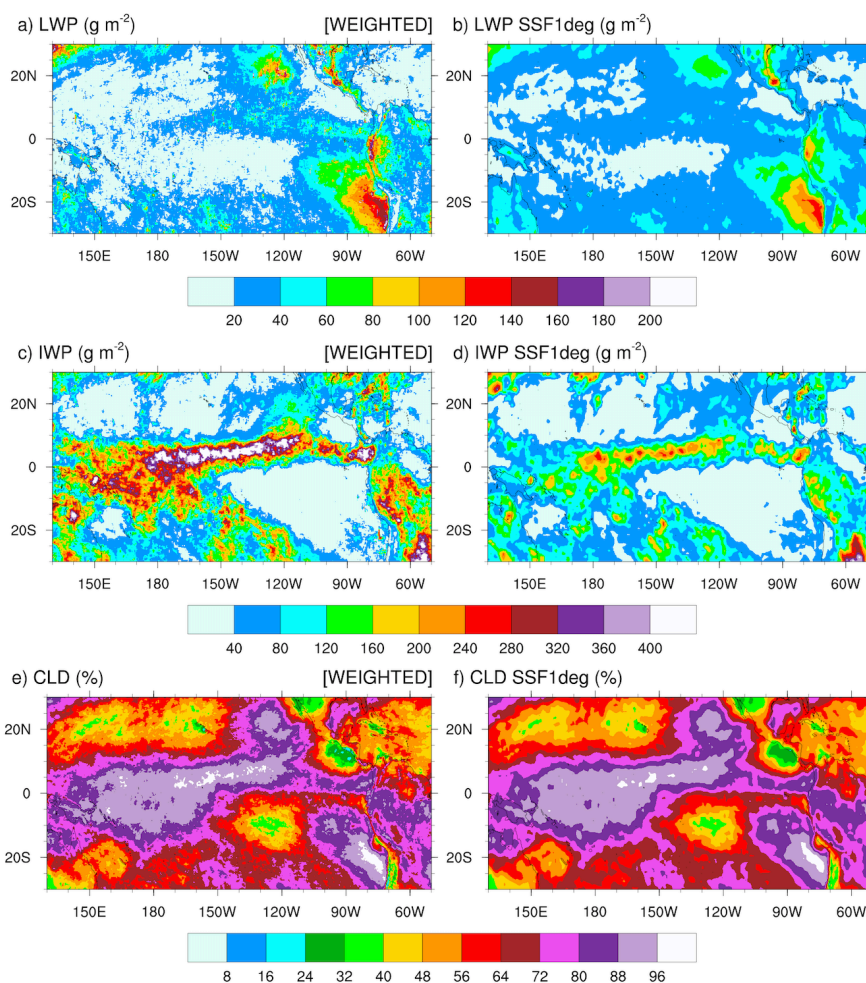
415
416   **Figure 5:** Monthly-mean cloudy area-weighted cloud liquid water path (LWP, top panels), cloudy-area weighted cloud ice water
417   path (IWP, middle panels), and cloud fraction (CLD, bottom panels) over the Tropical Pacific Ocean for December 2015. Panels
418   a), c), and e) are SSF data; panels b), d), and f) are SSF1deg climatological data.

419   Using ice water content data from the ascending (daytime) and descending (nighttime) portion of CloudSat orbits,

420   Waliser et al. (2009; Fig. 7) estimate that day-night fluctuations in the ice water content at 215 hPa account for as

421   much as 13% (20 %) of the annual mean ice water content over the warm pool (Tropical Eastern Pacific), in response

422   to the diurnal cycle of deep convection over the tropical oceans. Therefore, when computing the monthly-mean CF,

423   LWP, IWP, TOALW, and TOASW produced with GFu, GFv, MSKFu and MSKFv, we first sample the hourly model

424   diagnostics in accordance with the Aqua and Terra satellite orbits in order to reduce biases from different diurnal

425   sampling between our experiments and SSF data. Because the MODIS-based retrieval of the LWP and IWP is

426   insensitive to precipitation, and the rain, snow, and graupel mixing ratios are prognostic variables in THOM and fall

427   through the atmosphere at finite velocities, we infer that the LWP and IWP must include all precipitating and non-

428   precipitating condensates.

429   In addition to CERES SSF data, we use the monthly-mean precipitation rates from the TRMM Multisatellite

430   Precipitation Analysis (TMPA Version 7; Huffman et al., 2007) to compare simulated versus observed precipitation

431   rates, and monthly mean ERA-Interim reanalyses (Dee et al., 2011) to compare simulated versus observed precipitable

432   water in the lower troposphere.

4   Simulated versus satellite-retrieved precipitation

4.1   Incidence of subgrid-scale shallow and deep convection

435   Differences in the treatment of interactions between shallow and deep convection in GF and MSKF, as described in

436   Section 2, are bound to modify the partitioning between shallow and deep convection as spatial resolution increases

437   over the refined area of the mesh. A useful diagnostic to analyze the response of shallow and deep convection to local

438   mesh refinement is the incidence of convection. Because shallow convection in both GF and MSKF is non-

439   precipitating, we set the incidence of shallow convection to 100 % when cloud-tops of shallow convective updrafts

440   are detected, and 0 % otherwise. We set the incidence of deep convection to 100 % when convective precipitation

441   occurs and 0 % otherwise. Figures 6 and 7 highlight the impact of the horizontal scale dependence of convection on

442   the monthly-mean incidence of subgrid-scale shallow and deep convection in our uniform- and variable-resolution

443   experiments for December 2015.

444   Figure 6 shows that simulated shallow convection occurs over the entire Tropical Pacific, and that its incidence

445   is about twice as large in GFu and GFv as in MSKFu and MSKFv. In GFu and GFv, incidence in excess of 48 %

446   covers most of the Tropical Pacific, including the ITCZ and warm pool where GF allows shallow and deep convection

447   to occur simultaneously. GFu and GFv exhibit highest incidence of shallow convection off the coast of Peru where

448   persistent low-level stratiform clouds are formed. In contrast, the incidence of shallow convection in MSKFu and

449   MSKFv never exceeds 32 % over the entire domain and is less than 16 % over the ITCZ and warm pool where shallow

450   and deep convection are not allowed to coexist in MSKF. The bottom panels highlight differences in the incidence of

451   shallow convection between GFv and GFu, and MSKFv and MSKFu. Despite the fact that GF does not include a

452   spatial scale dependence in its formulation of shallow convection, GFv produces reduced shallow convection relative

453   to GFu over most of the Tropical Pacific, except most notably immediately off the coast of Peru. In contrast to GFv,

454   MSKFv yields increased incidence of shallow convection over most of the warm pool region. In MSKF, the height of

455   deep convective clouds decreases as horizontal resolution increases. As the classification between deep and shallow

456   convection is a function of cloud depth, convective clouds originally defined as deep are reclassified as shallow,

457   leading to increased incidence of shallow convection in the refined area of the mesh.
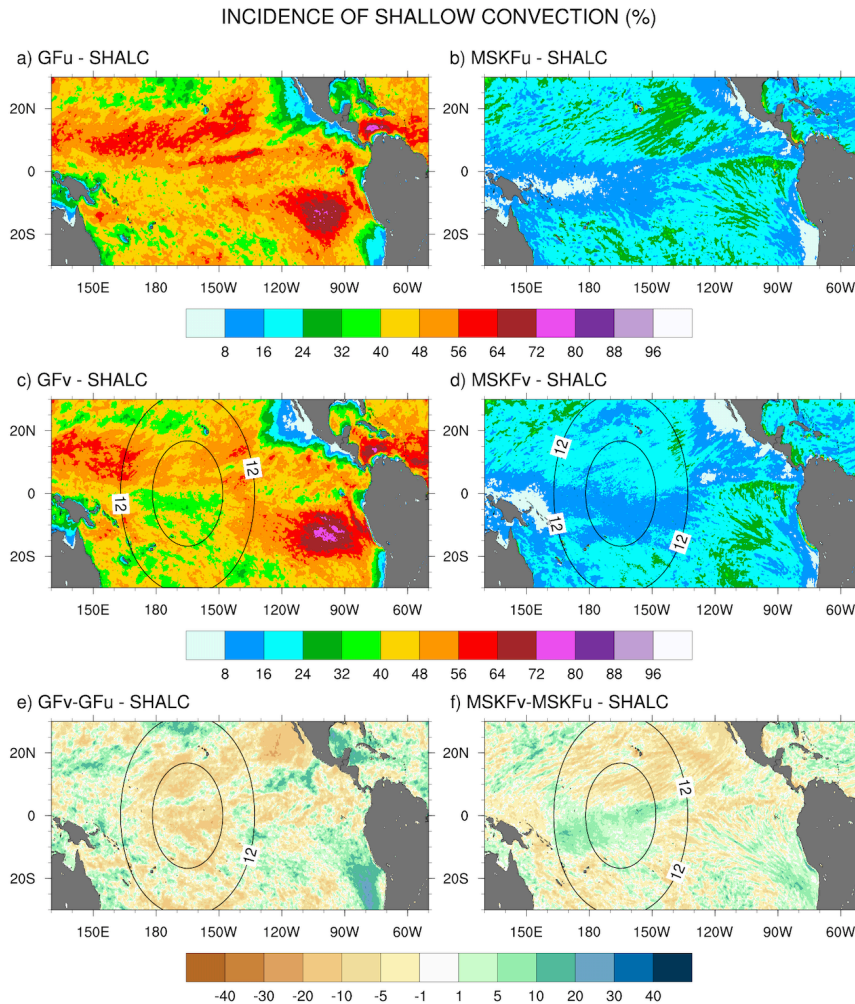
Figure 6: Monthly-mean incidence of shallow convection (SHALC) over the Tropical Pacific Ocean simulated in GFu and MSKFu (top panels) and GFv and MSKFv (middle panels), and difference in the incidence of shallow convection between GFv and GFu (bottom left panel) and MSKFv and MSKFu (bottom right panel) for December 2015.

In Fig. 7, the top and middle panels show that, in contrast to shallow convection, the incidence of deep convection has the same order of magnitude in GFu and MSKFu, and GFv and MSKFv. The top panels reveal that the incidence of deep convection is higher in MSKFu than GFu over the ITCZ and warm pool. In MSKFu, a sharp transition between areas of high and low incidence of deep convection causes areas outside of the ITCZ and warm pool to be mostly void of deep convection, as seen between 10°N and 30°N. In GFu, the incidence of deep convection is decreased over the warm pool relative to the ITCZ west of 160°W. Outside of the ITCZ and warm pool, GFu and GFv lead to higher incidence of deep convection than MSKFu and MSKFv because, in contrast to MSKF, GF allows deep and shallow convection to coexist in the same grid-cell. Middle panels highlight decreased incidence of subgrid-scale deep convection inside the refined area of the mesh over the warm pool in both GFv and MSKFv, as we expect clouds to

471   be resolved on the higher resolution grid, in conjunction with increased incidence east and west of the refined area.

472   The decreased incidence in the refined area is more pronounced between MSKFu and MSKFv than between GFu and

473   GFv whereas the upscaling impact of spatial refinement outside the refined area is greater in GFv than MSKFv. The

474   scale-aware formulation in GF does not produce the same contrast between the refined and coarse mesh in GFv and

475   GFu as that in MSKF in MSKFv and MSKFu. Fig. 7.f reveals a reduced incidence in excess of 25 % between MSKFu

476   and MSKFv starting at resolutions higher than 12 km flanked by increased incidence of deep convection east and west

477   of the refined area. In contrast, Fig. 7.e displays a longitudinal band of decreased incidence of deep convection between

478   90°W and the dateline, bordered by increased deep convection north of the equator and south of 10°S. Table 2 lists

479   the area-averaged incidence of deep and shallow convection over an area located inside the refined mesh (REFINED:

480   0.1°N to 5.1°N; 150°W to 180°W) and over the Tropical Eastern Pacific (EAST: 3.1°N to 8.1°N; 90°W to 120°W).
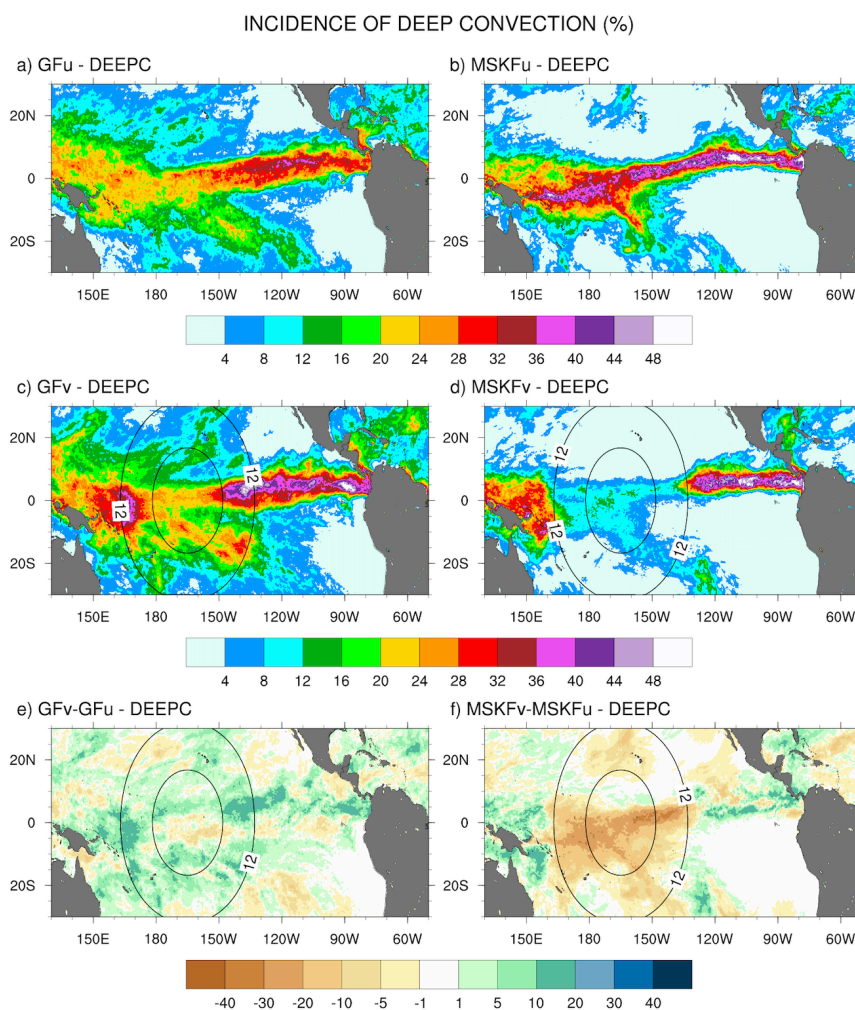
481
482   **Figure 7:** As Fig. 6, but for the monthly-mean incidence of deep convection (DEEPC).

483   Table 2 summarizes our results displayed in Figs. 6 and 7. The REFINED and EAST areas display little variation in
484   the incidence of shallow convection in any of the experiments. The incidence of shallow convection in GFu and GFv
485   is much higher than in MSKFu and MSKFv. The incidence of subgrid-scale deep convection is increased in the EAST
486   area relative to the REFINED area. Over the refined area, the incidence of subgrid-scale deep convection remains
487   about the same between GFu and GFv while strongly decreases between MSKFu and MSKFv.
488

	DEEP CONVECTION		SHALLOW CONVECTION	
	REFINED	EAST	REFINED	EAST
GFu	20	30	52	52
GFv	23	36	47	48
MSKFu	27	33	14	17
MSKFv	10	36	17	15

489   **Table 2:** Area-averaged incidence of deep and shallow convection. Units are %.

490   As described in Section 2, MSKF differentiates shallow from deep convection as a function of the convective
491   cloud depth. As spatial resolution increases, the scale aware formulation leads to a reduction in the intensity of
492   convection and depth of convective clouds, mostly deep convection, over the refined area as seen in Fig. 7.f. As the
493   depth of convective clouds originally classified as precipitating deep convective clouds become shallower, MSKF
494   reclassifies those same clouds as nonprecipitating shallow clouds, leading to near-equal compensation between the
495   decreased and increased incidence of deep and shallow convection over the warm pool. In contrast to MSKF, GF
496   causes precipitating deep convection to become precipitating shallow convection at increased spatial resolution. As
497   this process occurs in the deep convection scheme and both cloud types precipitate, variations in the incidence of deep
498   convection between GFu and GFv are small. Further analysis of the response of shallow convection between GFu and
499   GFv over the refined area is beyond the objectives of this research.

500   **4.2   Precipitation rates**

501   Figures 8 and 9 show the monthly-mean convective and grid-scale precipitation rates simulated in GFu and MSKFu
502   (top panels) and GFv and MSKFv (bottom panels). The top panels highlight similar geographical patterns of
503   convective and grid-scale precipitation rates in GFu and MSKFu. Between 80°W and 160°W, increased convective
504   and grid-scale precipitation rates are located over the ITCZ, in conjunction with increased incidence of deep
505   convection seen in Fig. 7.a,b. West of 160°W, GFu leads to decreased but more widespread convective precipitation
506   relative to MSKFu over the warm pool, in conjunction with decreased but more widespread incidence of convection.
507   In contrast to convective precipitation, there are few differences in grid-scale precipitation between GFu and MSKFu
508   (Figs. 9.a,b). This result infers that while deep convection is not triggered as often over the warm pool as over the
509   ITCZ, the amount of convective precipitation produced in one time-step is higher over the warm pool than over the
510   ITCZ, so that convective precipitation rates remain about the same in both regions. This result may also explain the

511   decrease in grid-scale precipitation over the warm pool compared to the ITCZ, as increased convective drying inhibits
512   grid-scale cloud microphysics processes and precipitation in the lower troposphere. In Fig. 8, and in agreement with
513   the middle panels of Fig. 7, bottom panels show that the scale-aware formulation in MSKF reduces convective
514   precipitation more efficiently than GF, leading to precipitation rates that are systematically smaller in MSKFv than
515   GFv in the refined area. The upscaling effect of spatial refinement produces different convective precipitation patterns
516   between MSKFv and GFv over the coarse area of the mesh. In GFv, increased incidence of deep convection on each
517   side of the refined area leads to increased convective precipitation and strongly decreased grid-scale precipitation in
518   the warm pool and Tropical Eastern Pacific, as seen in Figs. 8.c and 9.c. In contrast to GFv, MSKFv yields similar
519   convective (grid-scale) precipitation as MSKFu over those two areas, when comparing Fig. 8.b to Fig 8.d (Fig. 9.b to
520   Fig. 9.d). Over the refined area, grid-scale precipitation increases to compensate for the decrease in convective
521   precipitation in GFv and MSKFv so that total precipitation remains about the same between GFu (MSKFu) and GFv
522   (MSKFv). Comparing Fig. 9.c (Fig. 9.d) against Fig. 9.a (Fig. 9.b) reveals that grid-scale precipitation increases the
523   most along the ITCZ in conjunction with the greatest decrease in convective precipitation. GFv and MSKFv also lead
524   to an increase in grid-scale precipitation over the SPCZ, more so in MSKFv than GFv. MSKFv does not produce as
525   drastic a reduction in grid-scale precipitation as GFv over the coarse area of the mesh, indicating a smaller upscaling
526   impact of the refined mesh in MSKFv than GFv.
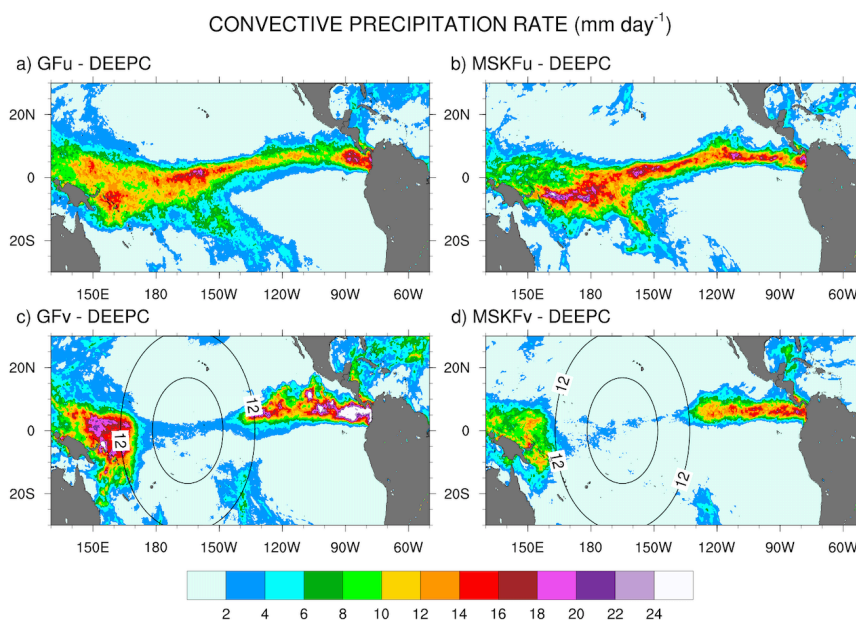
527
528   **Figure 8:** Monthly-mean convective (DEEPC) precipitation rate over the Tropical Pacific Ocean simulated in GFu and MSKFu
529   (top panels) and GFv and MSKFv (bottom panels) for December 2015.
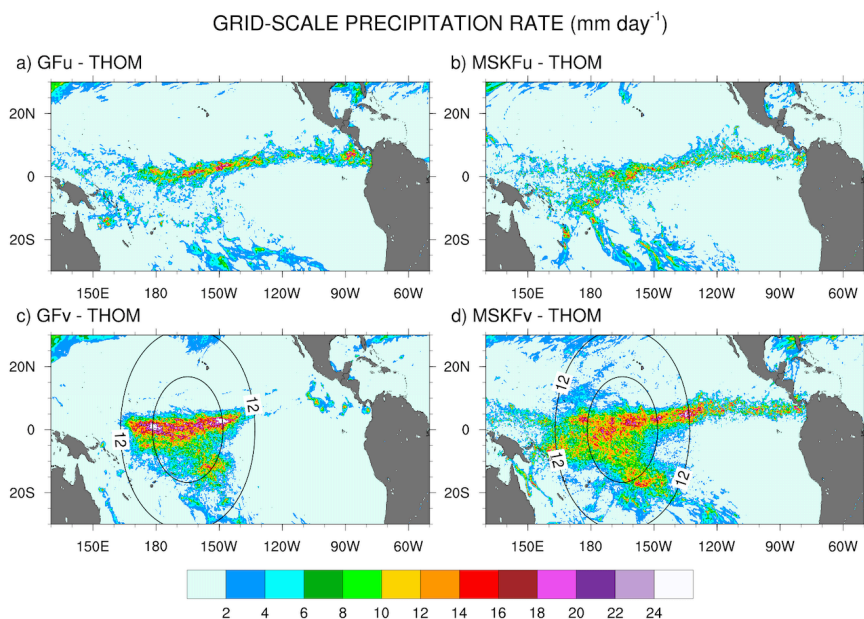
Figure 9: As Fig. 8, but the monthly mean grid-scale (THOM) precipitation rate.

The simulated total precipitation rate can be evaluated to observed TMPA precipitation using Figs. 10 and 11 which show the precipitation rates and differences between simulated and observed precipitation rates, respectively. Areas of maximum satellite-retrieved precipitation are found over the ITCZ between 130°W and the dateline (Fig. 10.a). Observed precipitation decreases over the warm pool west of the dateline and decreases strongly along the Tropical Eastern Pacific (between 80ºW and 120ºW) and the SPCZ. The four simulations overestimate precipitation in the Tropical Eastern Pacific between 80ºW and 120ºW (Figs. 10.b,e) with biases in excess of 11 mm day^{-1} (Figs. 11.a,d). The four simulations also overestimate precipitation between 130ºE and 160ºE, or west of the refined area, with biases about as large as those seen east of the refined area, except for MSKFu. The uniform-grid MPAS results (Figs. 10.b,c) display the highest precipitation rates over the area of warmest SSTs where we expect deepest convection to occur and are in reasonable agreement with TMPA data. However, GFu and MSKFu locate the ITCZ south of its observed location (Fig. 11.a,b), producing a positive bias straddling the Equator and a negative bias north of the Equator. The scale-aware dependence of deep convection in GF leads to decreased total precipitation in GFv compared to GFu over the entire refined area (Fig. 11.e). In contrast, Fig. 11.f shows that while the scale-aware dependence in MSKF leads to decreased precipitation in MSKFv over a major fraction of the refined area, it also leads to an improved location of the simulated ITCZ, as evidenced by increased precipitation north of the Equator.

547
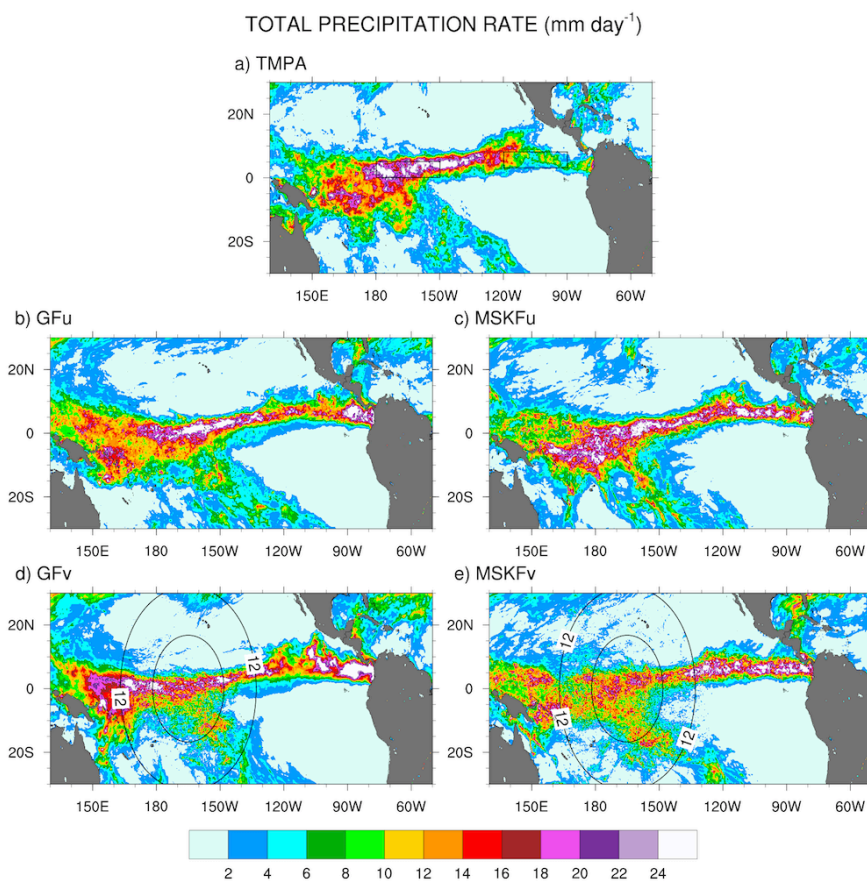
Figure 10: Monthly-mean total precipitation rate over the Tropical Pacific Ocean from TMPA data (top panel) and simulated with
GFu and MSKFu (middle panels) and GFv and MSKFv (bottom panels) for December 2015.

Table 3 summarizes the area-mean monthly-mean convective, grid-scale, and total simulated and observed TMPA
precipitation rates over the REFINED and EAST areas. Over the REFINED area, the total precipitation is about the
same in all four experiments, but less than that from TMPA data. This bias results because the simulated ITCZ is
located south of that actually observed (see Fig. 11). Total precipitation is reduced by 2.1 (2.3) mm day^{-1} between
GFu (MSKFu) and GFv (MSKFu), highlighting a near-equal compensation between decreased convective and
increased grid-scale precipitation rates as horizontal resolution increases. GFu and MSKFu, and GFv and MSKFv,
have similar partitioning between convective and grid-scale precipitation rates. Table 3 quantifies the increased
(decreased) convective (grid-scale) precipitation between GFu and GFv observed outside of the refined mesh in Fig.
6. For the EAST area, Table 3 shows that total precipitation increases by 2.7 (1.2) mm day^{-1} in conjunction with a 5.3
(0.5) mm day^{-1} increase in convective precipitation between GFu and GFv (MSKFu and MSKFv), highlighting the
impact of the refined area on the coarse area of the mesh in GFv and MSKFv.
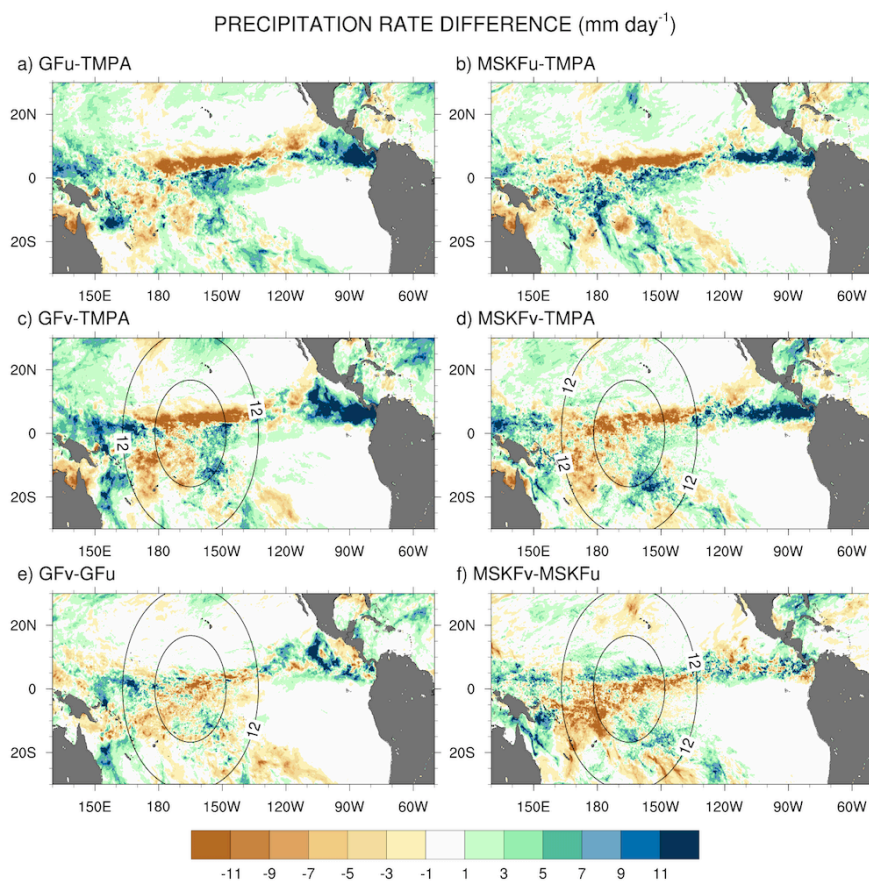
Figure 11: Monthly-mean precipitation rate difference over the Tropical Pacific Ocean between GFu (MSKFu) and TMPA data (top panels), GFv (MSKFv) and TMPA data (middle panels), and between GFv (MSKFv) and GFu (MSKFu) (bottom panels) for December 2015.

In summary, the scale dependence of convection in GF and MSKF produces the same partitioning between convective and grid-scale precipitation inside the refined area or decreased convective and compensating increased grid-scale precipitation as horizontal resolution increases. The upscaling impact on convective and grid-scale precipitation varies between GF and MSKF. As seen in Fig. 8 and Table 3, convective precipitation increases strongly over the warm pool and Eastern Pacific starting across the transition zones east and west of the refined area in GFv. In contrast, while the parameterization of the scale dependence of deep convection in MSKF produces a stronger decrease in convective precipitation in MSKFv than GFv, it produces a smoother transition in convective precipitation and decreased upscaling effect as spatial resolution reaches 30 km

573

	CONVECTIVE		GRID-SCALE		TOTAL	
	REFINED	EAST	REFINED	EAST	REFINED	EAST
GFu	10.0	8.7	6.1	3.7	16.1	12.4
GFv	1.9	14.0	12.1	1.1	14.0	15.1
MSKFu	10.9	10.6	4.9	4.76	15.8	15.3
MSKFv	1.7	11.1	11.8	5.4	13.5	16.5
TMPA					20.7	7.3

574 **Table 3:** Area-averaged convective, grid-scale, and total precipitation rates over the same areas as those described for Table 2.
575 Units are mm day^{-1}.

5 Simulated relative humidity and simulated versus satellite-retrieved LWP and IWP

5.1 Relative humidity

578 One effect of local mesh refinement is the decreased contribution of parameterized convection compensated by
579 increased contribution of grid-scale cloud microphysics to condensation processes and cloud formation with
580 increasing spatial resolution. Therefore, prior to comparing the simulated LWP and IWP against SSF data, we first
581 investigate differences in relative humidity (RH) between our uniform- and variable-resolution experiments. Figure
582 12 displays the monthly-mean longitude-pressure cross sections of RH latitudinally-averaged between 5°S and 5°N.
583 East of 150°W over the Tropical Eastern Pacific, the four experiments display similar vertical distributions of RH,
584 with relatively lower RH between 700 hPa and 150 hPa and higher RH in the PBL below 700 hPa and in the upper-
585 troposphere above 150 hPa. All four experiments show significant increase in RH west of 150°W across the entire
586 troposphere, over the warm pool where the warmest SSTs are seen (Fig. 2.a) and deepest convective updrafts are
587 formed. Comparing GFu against MSKFu over the warm pool shows that GF has stronger drying than MSKF in the
588 lower troposphere, leading to a lower RH between 850 hPa and 300 hPa in GFu than MSKFu. In addition, GF produces
589 stronger moistening than MSKF in the upper troposphere leading to a higher RH between 300 hPa and 100 hPa in
590 GFu than MSKFu. As seen in the bottom panels of Fig. 12, reducing parameterized deep convection while enhancing
591 grid-scale cloud microphysics produces a higher RH over the refined area in GFv and MSKFv, but without
592 significantly modifying RH over the coarse area of the mesh. Variations in the vertical distribution of RH at pressures
593 less than 400 hPa are more pronounced between GFu and GFv than between MSKFv and MSKFu. Because the cloud
594 fraction (CF) is a function of RH, as described in Xu and Randall (1996; Eq. 1), there is a strong relationship between
595 the longitude-pressure cross sections of RH and CF, as seen in Fig. S2 (see supplemental figures). The highest CF
596 coincide with the highest RH at about 100 hPa over the warm pool in all four experiments. As for RH, GFu and GFv
597 display higher and lower values of CF than MSKFu and MSKFv in the upper and lower troposphere. The top and
598 bottom panels of Fig. S3 show differences in RH and CF between GFv and GFu, and between MSKFv and MSKFu.

599   One notable difference is a stronger increase in upper-tropospheric clouds between MSKFu and MSKFv than between
600   GFv and GFu, particularly over the refined area of the mesh. While increased grid-scale condensation over the refined
601   area impacts the entire tropospheric in GFv, it more strongly affects the upper-troposphere in MSKFv.
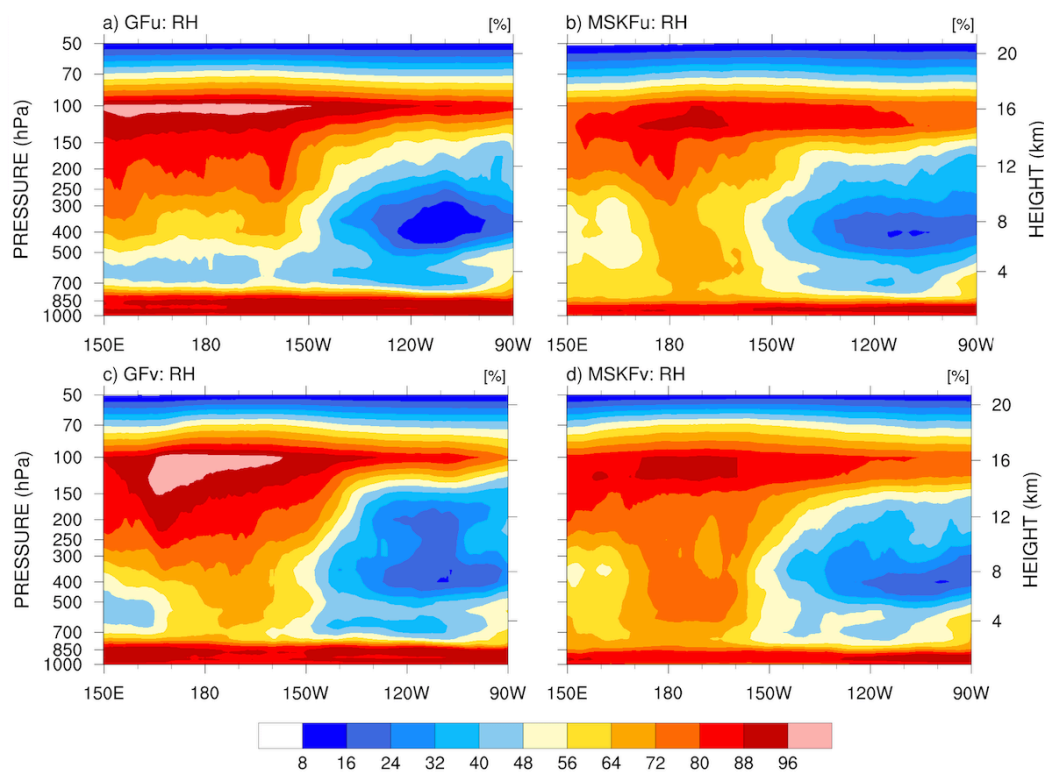
602
603   **Figure 12:** Longitude versus pressure cross-section of latitudinally-averaged relative humidity (RH) across the Tropical Pacific
604   Ocean simulated in GFu and MSKFu (top panels) and GFu and GFv (bottom panels) for December 2015.

605   To explain the change in RH over the refined area between the uniform- and variable-resolution experiments, we
606   compare the monthly-mean upward moisture flux at 850 hPa and 200 hPa between MSKFu and MSKFv over the
607   Tropical Eastern Pacific (Fig. 13). There is a significant decrease in the upward moisture flux between 850 hPa and
608   200 hPa in conjunction with decreased specific humidity with height in MSKFu and MSKFv (Fig. 12). As seen in the
609   top panels of Fig. 13, MSKFu yields highest values of the upward moisture flux along the ITCZ and over the warm
610   pool in association with parameterized deep convection. Outside the ITCZ and warm pool, lower values of the upward
611   moisture flux at 850 hPa result because of reduced deep convection in conjunction with shallow convection, as seen
612   over the SPCZ. At increased spatial resolution, convective processes transition from being parameterized to resolved,
613   producing larger grid-scale vertical velocities, stronger upward moisture flux, and increased grid-scale condensation
614   through the entire troposphere over the refined area of the mesh. Comparing the bottom versus top panels of Fig. 13
615   outlines the intensification of vertical moisture transport at both pressure levels over the refined area, leading to the
616   increased relative humidity with increased spatial resolutions shown in Fig. 12.
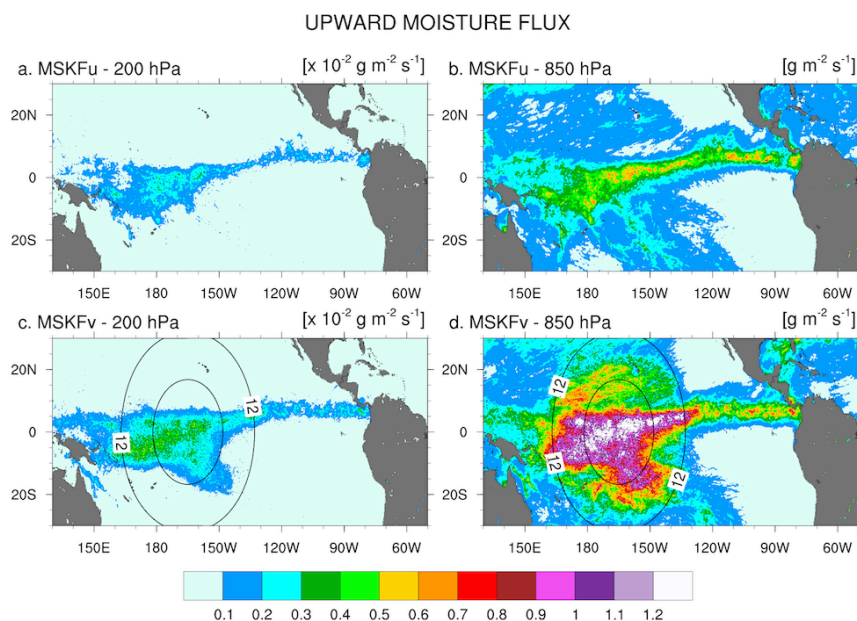
Figure 13: 200 hPa (left panels) and 850 hPa (right panels) monthly-mean upward moisture flux simulated with MSKF over the Tropical Pacific Ocean for December 2015. Top panels are for MSKFu and bottom panels are for MSKFv. Note the 1×10^{-2} scaling between 200 hPa and 850 hPa.

5.2 Liquid Water Path (LWP)

The LWP from the four simulations (Fig. 14) is evaluated with satellite-derived LWP (shown in Fig. 5) as well as compared among the simulations. In Fig. 14, the LWP is calculated using only the grid-scale cloud liquid water mixing ratio from THOM. Separate analyses would show that adding the prognostic grid-scale rain mixing ratio to the simulated LWP further increases biases when compared against the SSF LWP (not shown for brevity). We also did not include the contribution of the convective cloud liquid water mixing ratio to the LWP which is small compared to that from grid-scale cloud microphysics. Comparing Fig. 14.a with Fig. 5.a highlights that GFu strongly overestimates the LWP over the ITCZ, and between 20°N (20°S) and the northern (southern) limits of our analysis. As seen in Fig. 6, GFu attempts to form low-level boundary layer clouds off the coast of Peru but these clouds form too far west from the coast when compared against observations. This same bias is depicted in Fig 14.a since these low-level boundary layer clouds are characterized by high LWP. Fig. 14.b shows that the LWP is strongly decreased in MSKFu compared to GFu. If we set aside that MSKFu is unable to simulate low-level clouds off the Baja Peninsula and coast of Peru, the magnitude and regional patterns of the LWP simulated in MSKFu is in relatively good agreement with the SSF LWP. Because MSKF does not allow deep and shallow convection to coexist within the same grid-cell and deep convection dominates shallow convection over the ITCZ and warm pool, we suggest that detrained convective cloud water from deep convection as a source to grid-scale microphysics contributes a major part to the LWP produced by MSKFu (Fig. 14.b). The bottom panels of Fig. 14 reveal that the mesh refinement impacts the LWP simulated with MSKF more effectively than that simulated with GF inside and outside the refined area. This result is in agreement

639   with the stronger increase in RH between MSKFu and MSKFv than between GFu and GFv at lower levels. MSKFv

640   yields an increased LWP relative to MSKFu over the entire refined area (Fig. 14.f). MSKFv also has increased LWP

641   compared to MSKFu over the coarse area, but not as large as that seen over the refined area of the mesh. The LWP

642   predicted by GFu and GFv does not have a strong positive or negative trend, due to the fact that GF allows deep and

643   shallow convection to coexist within the same grid-cell of deepest convective activity, mainly over the ITCZ and

644   warm pool, and shallow convection does not account for variations in horizontal grid-spacing. While GFv mostly

645   leads to a decrease in the LWP between GFu and GFv over the coarse area, some grid cells inside the refined area

646   show a decrease in the LWP while other neighboring grid-cells show an increase in the LWP between GFu and GFv.

647   Over the coarse area, an obvious decrease in the LWP between GFv and GFu is seen over the ITCZ along the Tropical

648   Eastern Pacific as well as along the southern boundary of our analysis.
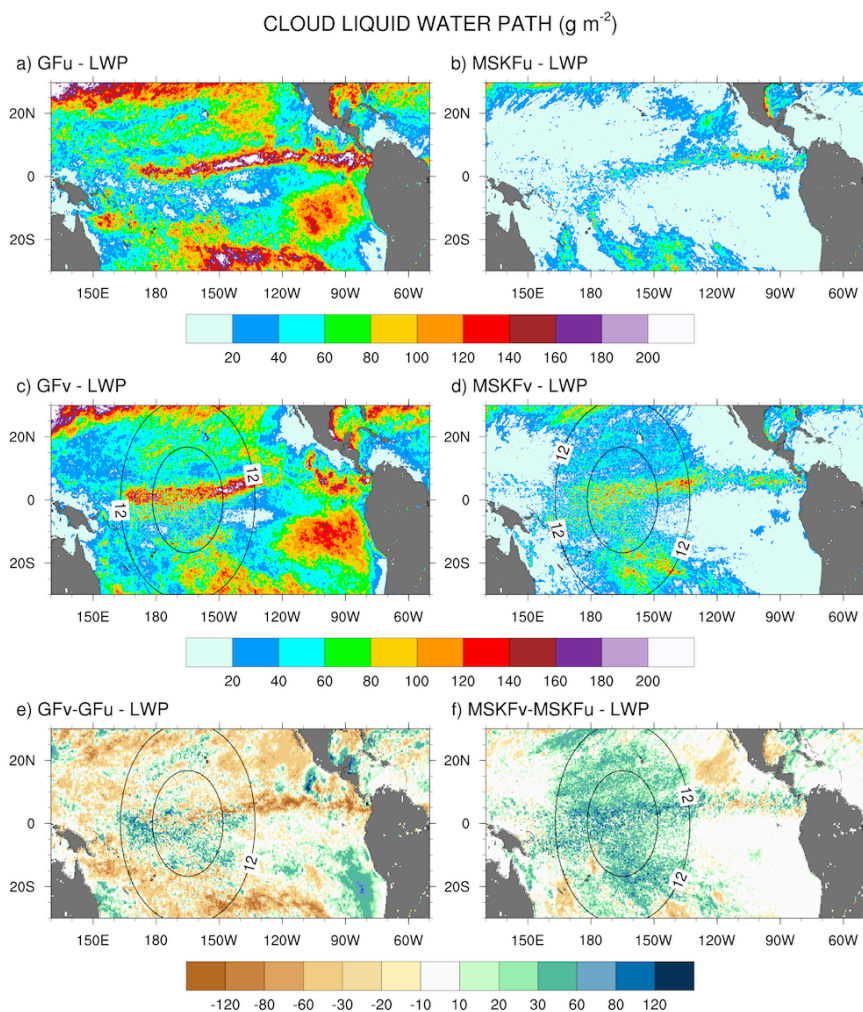
Figure 14: Monthly-mean cloud liquid water path (LWP) over the Tropical Pacific Ocean simulated with GFu and MSKFu (top panels) and GFv and MSKFv (middle panels), and monthly-mean LWP difference between GFv and GFu, and MSKFv and MSKFu (bottom panels) for December 2015.

In order to investigate the reasons why the LWP simulated in GFu strongly exceeds that from the SSF products and MSKFu, we calculate the monthly-mean LWP produced in grid-cells with incidence of deep convection, shallow convection, and without any kind of convection, using hourly outputs of the LWP from GFu. Comparing Fig. 15.a against Figs. 15.b and 15.c shows that a major fraction of the LWP over convectively active regions such as the ITCZ is actually produced at times when no convection is active or when only shallow convection is triggered. In contrast, the LWP produced in grid-cells with deep convection does not exceed 20 g m^{-2} at the scale used in Fig. 15. In GF, and in contrast to deep convection, shallow convection detrains total water as a source to grid-scale water vapor instead of water vapor, and cloud liquid and ice water separately. Because the detrained total water is treated as a source of water vapor, supersaturation conditions are more likely to persist and later removed by grid-scale condensation. In

662   contrast, detrainment from deep convective updrafts acts as a source of liquid water if temperatures are warmer than

663   258 K. Deep convection in conjunction with grid-scale condensation contributes the least to the LWP because updrafts

664   are taller than those formed from shallow convection, leading to condensation and deposition to occur at levels where

665   temperatures are colder than 258 K, and ice phase processes dominate.
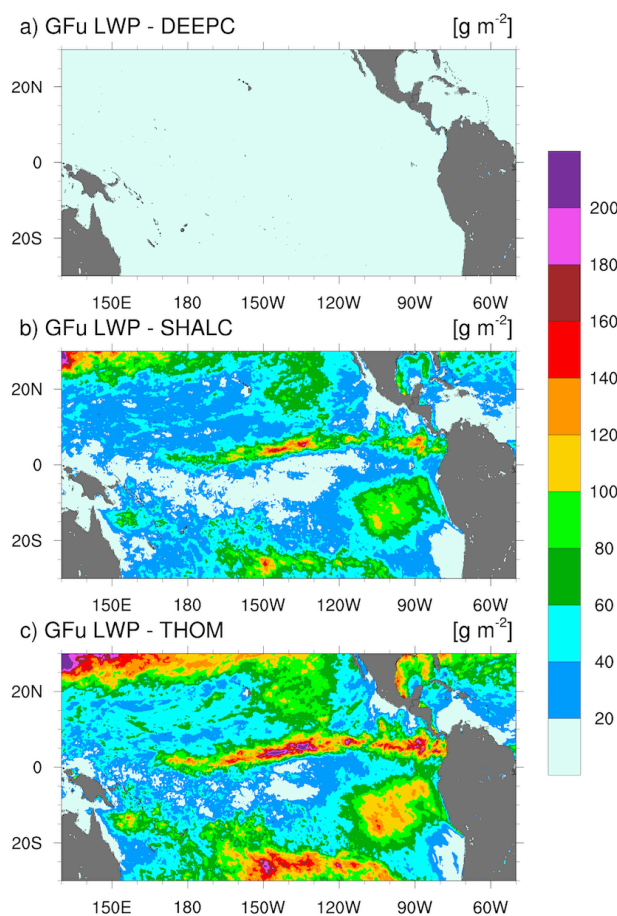
666
667   **Figure 15:** Monthly-mean of cloud liquid water path of corresponding to a) deep convection only (DEEPC); b) shallow convection
668   only (SHALC); and c) no convection (THOM) simulated with GFu over the Tropical Pacific Ocean for December 2015.

669   The impact of more active shallow convection in GFu and GFv relative to MSKFu and MSKFv is best seen in

670   Fig. 16 which shows differences between the monthly-mean precipitable water below 700 hPa from our experiments

671   and ERA-Interim (Dee et al., 2011) reanalyses. First, because varying horizontal resolution does not affect shallow

672   convection, the GFv and MSKFv results (Figs. 16.c, d) display similar biases as the GFu and MSKFu results (Figs.

673   16.a, b) over our entire analysis domain. Second, differences in the parameterization of shallow convection between

674   GF and MSKF lead GFu and GFv to produce significantly different biases than MSKFu and MSKFv against ERA-

675   Interim analyses. Over areas of deep convection, GFu and MSKFu exhibit a dry bias, implying that parameterized

676   deep convective updrafts are too strong and tend to overdry the lower atmospheric layers, as seen over the ITCZ, the

677   SPCZ, and warm pool. Over areas of shallow convection, GFu and MSKFu lead to increased and decreased

678   precipitable water below 700 hPa, in concordance with our earlier findings that GF and MSKF tend to overestimate
679   and underestimate the intensity of shallow convection respectively. Over the refined area, GFv and MSKFv produce
680   a negative bias, suggesting that reduced parameterized deep convection plus resolved grid-scale dynamics are as strong
681   in drying the lower troposphere as parameterized convection alone.

682
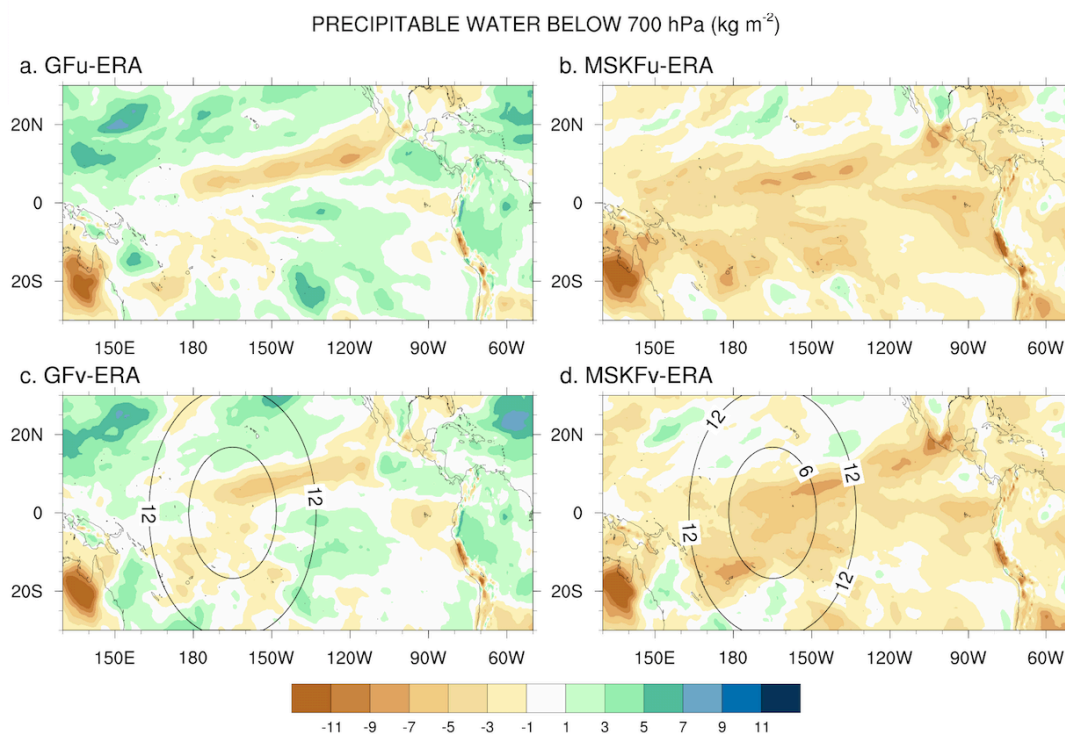
Figure 16: Monthly-mean difference between the simulated and ERA-Interim precipitable water below 700 hPa over the Tropical
Pacific Ocean for December 2015.

5.3   Ice Water Path (IWP)

686   Because MODIS is relatively insensitive to precipitation, the simulated IWP should comprise cloud ice, snow, and
687   graupel. Because graupel contributes a minor part to the IWP relative to cloud ice and snow and our results highlight
688   strong biases against SSF data, we do not include graupel in our computation of the simulated IWP. It is also important
689   to note that because THOM has the propensity to rapidly convert cloud ice to snow (Thompson et al. 2016), most of
690   the IWP is in the form of snow which falls at higher speeds than cloud ice, enhancing the depth of ice clouds. Lastly,
691   the middle panels of Fig. 5 show that our gridding and simple weighting of the IWP orbital data produce higher
692   monthly mean IWP than that from the official SSF1deg product. This result implies that biases between simulated and
693   satellite-derived IWP will be underestimated when using our SSF 0.2°x0.2° IWP data. Comparing GFu (MSKFu)
694   shown in Fig. 17 against the SSF IWP (Fig. 5.c) reveals that GFu (MSKFu) tends to underestimate (overestimate) the
695   IWP over the ITCZ and warm pool, and that GFu and MSKFu both overestimate the IWP along the west coast of
696   Central America. Comparing the top and middle panels of Fig. 17 highlights that MSKFu and MSKFv yield higher

697   IWP than GFu and GFv over the ITCZ and warm pool. Increased convective detrainment of cloud ice as a source of

698   grid-scale cloud ice to THOM in MSKFu than in GFv, due to the fact that partitioning between cloud liquid and ice

699   water starts at warmer temperatures in MSKFu than GFu, may be responsible to the increased IWP. The bottom panels

700   of Fig. 17 reveal that increasing spatial resolution worsens the simulated IWP compared to the SSF IWP over the

701   refined area in GFv and MSKFv. As shown in Fig. 12, mesh refinement over the warm pool produces higher upper-

702   tropospheric relative humidity leading to increased ice cloud microphysics. In contrast to GFv, MSKFv displays an

703   increase in the IWP over the coarse area of the mesh, showing a stronger upscaling effect of the refined area on the

704   coarse area of the mesh in MSKFv than GFv in the upper-troposphere.
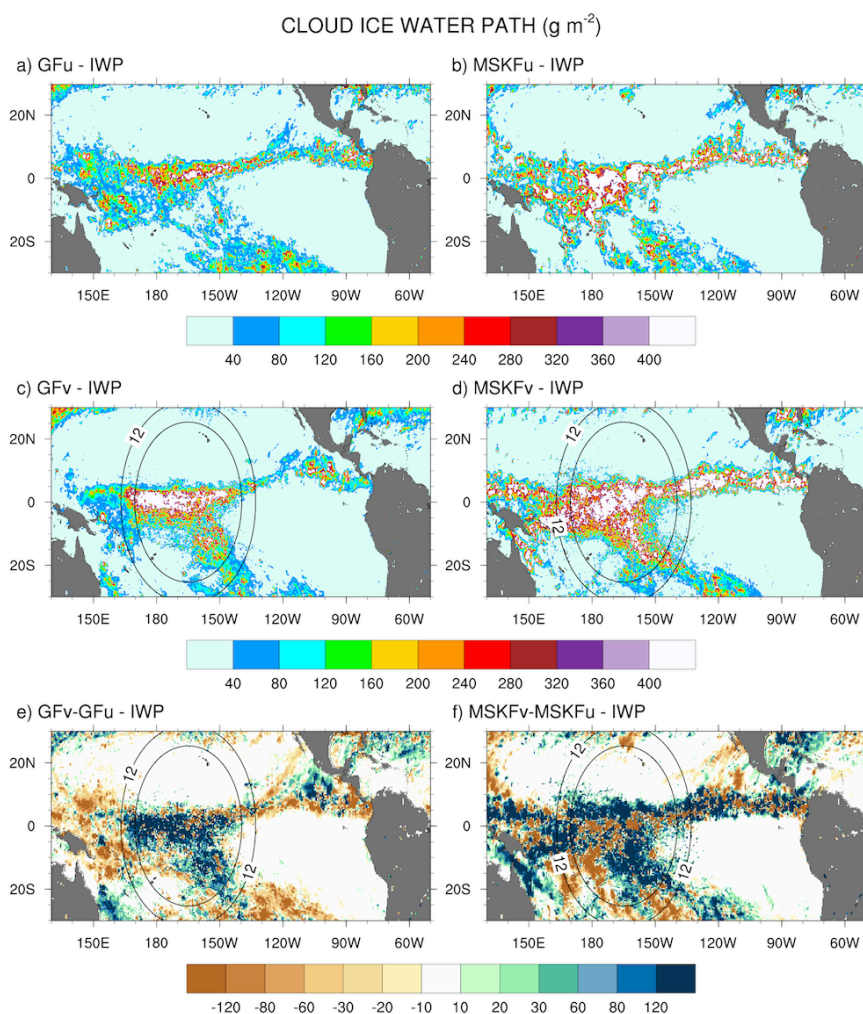
705

706   **Figure 17:** As Fig. 14, but for the cloud ice water path (IWP).

5.4   TOA radiation budget

708   Biases in the LWP and IWP introduce biases in the cloud fraction and cloud optical properties which in turn lead to

709   biases in the simulated TOALW and TOASW compared to CERES-SSF data. Figures S4, S5, and S6 display the

710   monthly-mean CF, TOALW, and TOASW from SSF data for December 2015 and the differences between the model

711   results and observations. Focusing on areas of deep convection over the ITCZ and warm pool, all four simulations

712   overestimate CF with larger biases seen in the GF than the MSKF experiments, and larger biases seen in the variable-

713   resolution than the uniform-resolution experiments. All four simulations also overpredict CF along the west coast of

714   Central America while underpredicting CF over areas of stratiform clouds along the west coast of South America and

715   Baja Peninsula. The impact of CF biases is that all four experiments underestimate the size of the warm pool and

716   width of the ITCZ, leading the TOALW (TOASW) to be too high (low) over areas of deep convection. These

717   differences are clearly linked to the differences noted in the LWP and IWP between MPAS and SSF data.

718   ## 6   Discussion and future research

719   Uniform- and variable-resolution experiments with two scale-aware parameterizations of deep and shallow convection

720   (GF and MSKF) in MPAS yield significant biases between simulated and satellite-derived monthly-mean precipitation

721   rates, LWP, IWP, and CF over the Tropical Pacific Ocean at horizontal resolutions of 30 km down to 6 km. Because

722   these biases affect cloud fraction and cloud optical properties, the four experiments present significant differences in

723   the TOALW and TOASW compared to CERES-SSF data for December 2015.

724   Precipitation simulated with the uniform-resolution experiments is overestimated compared to TMPA data. Biases

725   using GF are as large as those using MSKF, but part of the biases result because the simulated ITCZ is located south

726   of its observed location depicted as an area of maximum precipitation. Variable-resolution experiments do not yield

727   significant improvement in simulating precipitation. Inside the refined area, decreased convective precipitation plus

728   compensating increased grid-scale precipitation have the simulated total precipitation to exhibit similar biases between

729   our uniform- and variable-resolution experiments with both GF and MSKF. One major difference in using GF instead

730   of MSKF is the strong upscaling effect of the refined grid mesh on the coarse grid mesh, producing a strong increase

731   in convective precipitation east and west of the refined area of the mesh which did not exist in the MSKF. We plan to

732   further understand how the scale-aware formulation of deep convection in GF affect large-scale moist processes,

733   leading to increased triggering of convection over the coarse area of the mesh.

734   Differences in the simulated LWP between the uniform- and variable-resolution experiments using GF and MSKF

735   and against the CERES-SSF LWP highlight the need to revise the treatment of shallow convection in both convection

736   schemes and of its interactions with deep convection and cloud microphysics. While experiments using MSKF yield

737   the simulated LWP to be in reasonable agreement against that from the CERES-SSF product, those using GF yield

738   the simulated LWP to be strongly overestimated. Analyses show that the treatment of shallow convection in

739   conjunction with cloud microphysics processes explains most of the increased LWP in GFu and GFv compared to

740   MSKFu and MSKFv, and satellite-derived data. We propose to update our version of the GF shallow convection

741   scheme to that implemented in version 4.1 of the Advanced Research Weather Forecast (WRF) model. Because the

742 updated GF parameterization of shallow convection includes a revised cloud model that allows water vapor and cloud
743 liquid water to detrain separately and a fraction of the condensed water to precipitate, we propose to focus future
744 research on the impact of explicit detrainment of cloud liquid water and precipitation from shallow convective updrafts
745 on the simulated LWP in GF. Results show that MSKF underestimates shallow convection, leading the troposphere
746 below 700 hPa to be drier than actually observed. These results imply that the shallow convection parameterization in
747 MSKF needs to be updated or that a separate parameterization of shallow convection needs to be used in addition to
748 that in MSKF, which can be a part of our future study. The uniform- and variable-resolution experiments performed
749 here all overestimated the IWP compared to CERES-SSF data over the tropical Pacific region. This overprediction of
750 the IWP led to strong biases in the TOA long- and short-wave radiation budget compared to observations.

751 The scale-aware dependence of parameterized convection allows variable-resolution meshes spanning between
752 hydrostatic and nonhydrostatic scales to be used within a global framework. As horizontal resolution increases from
753 the coarse to refined area of the mesh, convection transitions from parameterized to resolved and grid-scale cloud
754 microphysics contribute a major part to moist processes over the refined grid mesh. Stronger grid-scale vertical
755 velocities associated with smaller grid-spacing over the refined area produce increased upward moisture flux and grid-
756 scale condensation, further increasing biases between the simulated and satellite-retrieved LWP, IWP, and clouds.
757 Our results show that mesh refinement over the Tropical Pacific Ocean does not systematically improve precipitation
758 and clouds, due to complicated interactions between convection, cloud microphysics, and radiation. As cloud
759 microphysics processes drive the moisture budget over the refined area of the mesh, we propose to expand this
760 diagnostic study to a process study by further understanding the cloud microphysics tendencies that need to be
761 improved with the aim to reduce discrepancies between model and observations. In that vein, the recently developed
762 MSKF that includes a double moment microphysics (Glotfelty et al., 2019) would be useful in a future process study.

765 *Code and data availability*: The source code used to initialize and run our experiments is based on MPAS-v5.2 which
766 is freely available from https://github.com/MPAS-Dev/MPAS-Model/releases/tag/v5.2. Modifications to the original
767 source code and scripts to run the experiments are available from https://doi.org/10.5281/zenodo.3515440 (Fowler,
768 2019) while initialization files, and outputs from the experiments are located on the NCAR Campaign Storage System.
769 These files can be made available by contacting the corresponding author. Examples of CERES SSF Aqua and Terra
770 orbital and gridded data, daily-mean and monthly-mean simulated diagnostics, and post-processing scripts are also
771 available from https://doi.org/10.5281/zenodo.3515440 (Fowler, 2019).

774 *Author contributions*: LF developed all the modifications that were made to the MPAS-v5.2 released version and were
775 necessary to run the different experiments. KA made all the updates to the MultiScale Kain-Fritsch parameterization
776 of convection. LF and MB designed the experiments, and LF conducted and analyzed the simulations. LF prepared
777 the manuscript with contributions from all co-authors.

779

780 *Competing interests*: The authors declare that they have no conflict of interest.

781

782

783 *Acknowledgments:* This research is based upon work supported by the National Center for Atmospheric Research

784 which is a major facility sponsored by the National Science Foundation under Cooperative Agreement No. 1852977.

785 The authors thank Dr. Hugh Morrison for his careful review and constructive suggestions of the manuscript prior to

786 its submission. The CERES-SSF data were obtained from the NASA Langley Research Center Atmospheric Science

787 Data Center. The TMPA data were acquired as part of the activities of NASA's Science Mission Directorate and are

788 archived and distributed by the Goddard Earth Sciences (GES) Data and Information Services Center (DISC). We

789 would like to acknowledge high-performance computing support from Cheyenne (doi:10.5065/D6RX99hX) provided

790 by NCAR's Computational and Information Systems Laboratory, sponsored by the National Science Foundation. We

791 acknowledge the use of the NCAR Command Language (Version 6.3.2) [Software]. (2019). Boulder, Colorado:

792 UCAR/NCAR/CISL/TDD. http://dx.doi.org/10.5065/D6WD3XH5 for all figures.

References

793

794 Alapaty, K., Herwehe, J.A., Otte, T.L., Nolte, C.G., Bullock, O.R., Ballard, M.S., Kain, J.S., and Dudhia, J.:
795   Introducing subgrid-scale cloud feedbacks to radiation for regional meteorological and climate modeling,
796   Geophys. Res. Lett., 39, L24809, https://doi.org/10.1029/2012GL054031, 2012.

797 Alishouse, J.C., Snider, J.B., Westwater, E.R., Swift, C.T., Ruf, C.S., Vongsathron, S.A., and Ferraro, R.R.:
798   Determination of cloud liquid water content using the SSM/I, IEEE T. Geosci. Remote, 28, 817-822,
799   https://doi.org/10.1109/36.58968, 1990.

800 Arakawa, A., and Schubert, W.H.: Interaction of a cumulus cloud ensemble with the large-scale environment, Part I,
801   J. Atmos. Sci., 31, 674-701, https://doi.org/10.1175/1520-0469(1974)031<0674:IOACCE>2.0.CO;2, 1974.

802 Arakawa, A., and Wu, C.-M.: A unified representation of deep moist convection in numerical modeling of the
803   atmosphere. Part I, J. Atmos. Sci., 70, 1977-1992, https://doi.org/10.1175/JAS-D-12-0330.1, 2013.

804 Bechtold, P., Bazile, E., Guichard, F., Mascart, P., and Richard, E.: A mass-flux convection scheme for regional and
805   global models, Q. J. Roy. Meteor. Soc., 130, 3139-3172, https://doi.org/10.1002/qj.49712757309, 2001.

806 Bechtold, P., Köhler, M., Jung, T., Doblas-Reyes, F., Leutbecher, M., Rodwell, M. J., Vitart, F., and Balsamo, G.:
807   Advances in simulating atmospheric variability with the ECMWF model: From synoptic to decadal time-scales,
808   Q. J. Roy. Meteor. Soc., 134, 1337–1351, https://doi.org/10.1002/qj.289, 2008.

809 Brown, J.M.: Mesoscale unsaturated downdrafts driven by rainfall evaporation: A numerical study, J. Atmos. Sci., 36,
810   313-338, https://doi.org/10.1175/1520-0469(1979)036<0313:MUDDBR>2.0.CO;2, 1979.

811 Chen, F., and Dudhia, J.: Coupling an advanced land surface-hydrology model with the Penn State-NCAR MM5
812   modeling system. Part I: Model implementation and sensitivity, Mon. Weather Rev., 129, 569-585,
813   https://doi.org/10.1175/1520-0493(2001)129<0569:CAALSH>2.0.CO;2, 2001.

814 Dee, D.P., and 35 co-authors: The ERA-Interim reanalysis: configuration and performance of the data assimilation
815   system, Q. J. Roy. Meteor. Soc., 137, 553-597, https://doi.org/10.1002/qj.828, 2011.

816 Dolinar, E.K., Dong, X., Xi, B., Jiang, J.H., and Su, H.: Evaluation of CMIP5 simulated clouds and TOA radiation
817   budgets using NASA satellite observations, Clim. Dynam., 44, 2229-2247, https://doi.org/10.1007/s00382-014-
818   2158-9, 2015.

819 Fowler, L.D.: experimentsMPAS-v5.2, Zenodo, https://doi.org/10.5281/zenodo.3515440, 2019.

820 Fowler, L.D., Skamarock, W.C., Grell, G.A., Freitas, S.R., and Duda, M.G.: Analyzing the Grell-Freitas convection
821   scheme from hydrostatic to nonhydrostatic scales within a global model, Mon. Weather Rev., 144, 2285-2306,
822   https://doi.org/10.1175/MWR-D-15-0311.1, 2016.

823 Frank, W.M., and Cohen, C.: Simulation of tropical convective systems. Part I: A cumulus parameterization, J. Atmos.
824   Sci., 44, 3787-3799, https://doi.org/10.1175/1520-0469(1987)044<3787:SOTCSP>2.0.CO;2, 1987.

825 Fritsch, J.M., and Chappell, C.F.: Numerical prediction of convectively driven mesoscale pressure systems. Part I:
826   Convective parameterization, J. Atmos. Sci., 37, 1722–1733, https://doi.org/10.1175/1520-
827   0469(1980)037<1722:NPOCDM>2.0.CO;2, 1980.

828 Geier, E.B., Green, R.N., Kratz, D.P., Minnis, P., Miller, W.F., Nolan, S.K., and Franklin, C.B.: Clouds and the Earth's
829   Radiant Energy System (CERES) data management system. Single Satellite Footprint TOA/Surface Fluxes and
830   Clouds (SSF) collection document. Release 2, Version 1, 243 pp, 2003.

831 Giorgetta, M.A., Brokopf, R., Crueger, T., Esch, M., Fiedler, S., Helmert, J., Hohenegger, C., Kornblueh, L., Köhler,
832   M., Manzini, E., Mauritsen, T., Nam, C., Raddatz, T., Rast, S., Reinert, D., Sakradzija, M., Schmidt, H., Schneck,
833   R., Schnur, R., Silvers, L., Wan, H., Zängl, G., and Stevens, B: ICON-A, the atmosphere component of the ICON
834   Earth System Model: I. Model description, J. Adv. Model. Earth Sy.10, 1613-1637,
835   https://doi.org/10.1029/2017MS001242, 2018.

836 Glotfelty, T., Alapaty, K., He, J., Hawbecker, P., Song, X., and Zhang, G.: The Weather Research and Forecasting
837   Model with aerosol cloud-interactions (WRF-ACI): Development, evaluation, and initial applications, Mon. Wea.
838   Rev., 147, 1491-1511, https://doi.org/10.1175/MWR-D-18-0267.1, 2019.

839 Greenwald, T.J., Stephens, G.L., Vonder Haar, T.H., and Jackson, D.L.: A physical retrieval of cloud liquid water
840   over global oceans using special sensor microwave/imager (SSM/I) observations, J. Geophys. Res., 98, 18471-
841   18488, https://doi.org/10.1029/93JD00339, 1993.

842 Grell, G.A: Prognostic evaluation of assumptions uses by cumulus parameterizations, Mon. Weather Rev., 121, 764-
843   787, https://doi.org/10.1175/1520-0493(1993)121<0764:PEOAUB>2.0.CO;2, 1993.

844 Grell, G.A., and Dévényi, D.: A generalized approach to parameterizing convection combining ensemble and data
845   assimilation techniques, Geophys. Res. Lett., 29, 38-1-38-4, https://doi.org/10.1029/2002GL015311, 2002.

846 Grell, G.A., and Freitas, S.R.: A scale and aerosol aware stochastic parameterization for weather and air quality
847   modeling, Atmos. Chem. Phys., 14, 5233-5250, https://doi.org/10.5194/acp-14-5233-2014, 2014.

848 Guo, H., Golaz, J.-C., Donner, L., Wyman, B. , Zhao, M., and Ginoux, P.: CLUBB as a unified cloud parameterization:
849   opportunities and challenges, Geophys. Res. Lett., 42, 4540-4547, https://doi.org/10.1002/2015GL063672, 2015.

850 He, J., and Alapaty, K.: Precipitation partitioning in multiscale atmospheric simulations: Impacts of stability
851   restoration methods, J. Geophys. Res., 123, 10185-10201, https://doi.org/10.1029/2018JD028710, 2018.

852 Herwehe, J.A., Alapaty, K. , and Bullock Jr., O.R: Evaluation of developments toward a multi-scale Kain-Fritsch
853   parameterization in WRF. 2014 Community Modeling and Analysis System Conference, Chapel Hill, NC, EPA,
854   2014.

855 Hong, S.-Y., and Lim, J.-O: The WRF single moment 6-class microphysics scheme (WSM6), J. Korean Meteor. Soc.,
856   42, 129-151, 2006.

857   Hong, S.-Y., Choi, J., Chang, E.-C. , Park, H., and Kim Y.-J.: Lower-tropospheric enhancement of gravity wave drag
858   in a global spectral atmospheric forecast model, Weather Forecast, 23, 523-531,
859   https://doi.org/10.1175/2007WAF2007030.1, 2008.

860   Huffman, G.J., Balvin, D.T., Nelkin, E.J., and Wolff, D.B.: The TRMM Multisatellite Precipitation Analysis (TMPA):
861   Quasi-global, multiyear, combined-sensor precipitation at fine scales, J. Hydrometeorol., 8, 38-55,
862   https://doi.org/10.1175/JHM560.1, 2007.

863   Iacono, M. J., Mlawer, E. J., Clough, S. A., and Morcrette, J.-J.: Impact of an improved longwave radiation model,
864   RRTM, on the energy budget and thermodynamic properties of the NCAR Community Climate Model, CCM3,
865   J. Geophys. Res., 105, 14 873–14 890, https://doi.org/10.1029/2000JD900091, 2000.

866   Jiang, J.H., Su, H., Zhai, C., Perun, V.S, Del Genio, A., Nazarenko, L.S., Donner, L.J., Horowitz, L., Seman, C., Cole,
867   J., Gettelman, A., Ringer, M.A., Rotstayn, L., Jeffrey, S., Wu, T., Brient, F., Dufresne, J.-L., Kawai, H., Koshiro,
868   T., Watanabe, M., L'Ecuyer, T.S., Volodin, E.M., Iversen, T., Drange, H., Mesquita, M.D.S., Read, W.G., Waters,
869   J.W., Tian, B., Teixeira, J., and Stephens, G.L.: Evaluation of cloud and water vapor simulations in CMIP5
870   climate models using NASA "A-Train" satellite observations, J. Geophys. Res., 117, D14105,
871   https://doi.org/10.1029/2011JD017237, 2012.

872   Ju, L., Ringler, T., and Gunzburger, M.: Voronoi tessellations and their applications to climate and global modeling,
873   Numerical Techniques for Global Atmospheric Models, P. Lauritzen et al., Eds., Springer, 313-342, 2011.

874   Kain, J.S.: The Kain-Fritsch parameterization: An update, J. Appl. Meteorol., 43, 170-181,
875   https://doi.org/10.1175/1520-0450(2004)043<0170:TKCPAU>2.0.CO;2, 2004.

876   Kain, J.S, and Fritsch, J.M.: A one-dimensional entraining/detraining plume model and its application in convective
877   parameterization, J. Atmos. Sci., 47, 2784-2802, https://doi.org/10.1175/1520-
878   0469(1990)047<2784:AODEPM>2.0.CO;2, 1990.

879   Kain, J.S., and Fritsch, J.M.: The role of convective "trigger function" in numerical forecasts of mesoscale convective
880   systems, Meteorol. Atmos. Phys., 49, 93-106, https://doi.org/10.1007/BF01025402, 1992.

881   Kain, J.S., and Fritsch, J.M.: Convective parameterization for mesoscale models: The Kain-Fritsch scheme, The
882   Representation of Cumulus Convection in Numerical Models, Meteor. Mon., No. 24, American Meteorological
883   Society, Boston, MA, 165-170, https://doi.org/10.1007/978-1-935704-13-3_16, 1993.

884   Kay, J.E., Deser, C., Phillips, A., Mai, A., Hannary, C., Strand, G., Arblaster, J.M., Bates, S.C., Danabasoglu, G.,
885   Edwards, J., Holland, M., Kushner, P., Lamarque, J.-F., Lawrence, D., Lindsay, K., Middleton, A., Munoz, E.,
886   Neale, R., Oleson, K., Polvani, L., and Vertenstein, M.: The Community Earth System Model (CESM) large
887   ensemble project, B. Am. Meteorol. Soc., 96, 1333-1349, https://doi.org/10.1175/BAMS-D-13-00255.1, 2015.

888   Kessler, E.: On the distribution and continuity of water substances in atmospheric circulation, Meteor. Mon., No. 10,
889   American Meteorological Society, Boston, MA, 1-84, https://doi.org/10.1007/978-1-935704-36-2_1, 1969.

890 Klemp, J.B.: A terrain-following coordinate with smoothed coordinate surfaces, Mon. Weather Rev., 139, 2163-2169,
891   https://doi.org/10.1175/MWR-D-10-05046.1, 2011

892 Klemp, J.B., Skamarock, W.C., and Dudhia, J.: Conservative split-explicit time integration methods for the
893   compressible   non-hydrostatic   equations,   Mon.   Weather   Rev.,   135,   2897-2913,
894   https://doi.org/10.1175/MWR3440.1, 2007.

895 Krishnamurti, T.N., Low-Nam, S., and Pasch, R.: Cumulus parameterization and rainfall rates II, Mon. Weather Rev.,
896   111, 815-828, https://doi.org/10.1175/1520-0493(1983)111<0815:CPARRI>2.0.CO;2, 1983.

897 Li, J.-L., Waliser, D., Woods, C., Teixeira, J., Bacmeister, J., Chern, J., Shen, B.-W., Tompkins, A., Tao, W.-K., and
898   Köhler, M.: Comparisons of satellites liquid water estimates to ECMWF and GMAO analyses, 20th century IPCC
899   AR4   climate   simulations   and   GCM   simulations,   Geophys.   Res.   Lett.,   35,   L9710,
900   https://doi.org/10.1029/2008GL035427, 2008.

901 Li, J.-L., Waliser, D.E., Chen, W.-T., Guan, B., Kubar, T., Stephens, G., Ma, H.-Y., Deng, M., Donner, L., Seman, C.
902   , and Horowitz, L.: An observational based evaluation of cloud ice water in CMIP3 and CMIP5 GCMs and
903   contemporary   reanalyses   using   contemporary   satellite   data,   J.   Geophys.   Res.,   117,   D16105,
904   https://doi.org/10.1029/2012JD017640, 2012.

905 Li, J.-L., Lee, S., Ma, H.-Y, Stephens, G., and Guan, B.: Assessment of the cloud liquid water from climate models
906   and   reanalysis   using   satellite   observations,   Terr.   Atmos.   Ocean.   Sci.,   29(6),   653-678,
907   https://doi.org/10.3319/TAO.2018.07.04.01, 2018.

908 Mahoney, K.M.: The representation of cumulus convection in high-resolution simulations of the 2013 Colorado front
909   range flood, Mon. Weather Rev., 144, 4265-4278, https://doi.org/10.1175/MWR-D-16-0211.1, 2016.

910 Meehl, G.A., Delworth, T.L., Latiff, M., McAveney, B., Mitchell, J.F.B., Stouffer, R.J., and Taylor. K.E.: The WCRP
911   CMIP3 multimodel dataset: A new era in climate change research, B. Am. Meteorol. Soc., 88, 1383-1394,
912   https://doi.org/10.1175/BAMS-88-9-1383, 2007.

913 Minnis, P., and coauthors: CERES Edition-2 cloud property retrievals using TRMM VIRS and Terra and Aqua
914   MODIS   data-Part   I: Algorithms,   IEEE   T.   Geosci.   Remote.,   Vol.   49,   NO   11,   4374-4400,
915   https://doi.org/10.1109/TGRS.2011.2144601, 2011.

916 Minnis, P., Kratz, D.P, Coakley, J.J.A., King, M.D., Garber, D., Heck, P., Mayor, S., Young, D.F., and Arduini, R.:
917   Cloud optical property retrieval (Subsystem 4.3), in Clouds and the Earth's Radiant Energy System (CERES)
918   Algorithm Theoretical Basis Document , Vol III, Clouds and Radiance Inversions (Subsystem 4), NASA RP
919   1376, edited by Science Team CERES, pp. 135-176, NASA, Washington D.C., 1995.

920 Mlawer, E. J., Taubman, S. J., Brown, P. D., Iacono, M. J., and Clough, S. A.: Radiative transfer for inhomogeneous
921   atmospheres: RRTM, a validated correlated-k model for the longwave, J. Geophys. Res., 102, 16663–16682,
922   https://doi.org/10.1029/97JD00237, 1997.

923   Molod, A., Takacs, L., Suarez, M., Bacmeister, J., Song, I.-S., and Eichman, A.: The GEOS-5 atmospheric general
924   circulation model: Mean climate from MERRA to Fortuna, Technical Report Series on Global Modeling and
925   Assimilations, Vol. 28, 124 pp, 2012.

926   Nakanishi, M., and Niino, H.: Development of an improved turbulence closure model for the atmospheric boundary
927   layer, J. Meteor. Soc. Japan, 87, 895–912, https://doi.org/10.2151/jmsj.87.895, 2009.

928   Ogura, Y., and Cho, H.-R.: Diagnostic determination of cumulus cloud populations from observed large-scale
929   variables,   J.   Atmos.   Sci.,   30,   1276-1286,   https://doi.org/10.1175/1520-
930   0469(1973)030<1276:DDOCCP>2.0.CO;2, 1973.

931   Olson, J.B., Kenyon, J.S., Angevine, W.M., Brown, J.M., Pagowski, M., and Suselj, K.: A description of the MYNN-
932   EDMF scheme and the coupling to other components in WRF-ARW, NOAA Technical Memorandum OAR GSD,
933   61, pp 37, 2019.

934   Platnick, S., King, M.D., Ackerman, S.A., Wenzel, W.P., Baum, B.A., Riedl, J.C. , and Frey, R.A.: The MODIS cloud
935   products: Algorithms   and   examples   from   Terra,   IEEE   T.   Geosci.   Remote,   41,   459-473,
936   https://doi.org/10.1109/TGRS.2002.808301, 2003.

937   Qiao, F., and Liang, X-Z: Effects of cumulus parameterization closures on the simulations of summer precipitation
938   over   the   United   States   coastal   oceans,   J.   Adv.   Model.   Earth   Sy.,   8,   764-785,
939   https://doi.org/10.1002/2015MS000621, 2015.

940   Raymond, D.J.: Regulation of moist convection over the west Pacific warm pool, J. Atmos. Sci., 52, 3945-3959,
941   https://doi.org/10.1175/1520-0469(1995)052<3945:ROMCOT>2.0.CO;2, 1995.

942   Schwarz, C.S.: Medium-range convection-allowing ensemble forecasts with a variable-resolution global model, Mon.
943   Weather Rev., 147, 2997-3023, https://doi.org/10.1175/MWR-D-18-0452.1, 2019.

944   Simpson, J., and Wiggert, V.: Models of precipitating cumulus towers, Mon. Weather Rev., 97, 471-489,
945   https://doi.org/10.1175/1520-0493(1969)097<0471:MOPCT>2.3.CO;2, 1969.

946   Skamarock, W.C., and Gassmann, A.: Conservative transport schemes for spherical geodesic grids: High-order flux
947   operators for ODE-based time integration, Mon. Weather Rev., 139, 2962-2975, https://doi.org/10.1175/MWR-
948   D-10-05056.1, 2011.

949   Skamarock, W.C., Klemp, J.B., Duda, M.G., Fowler, L.D., Park, S.-H., and Ringler, T.D.: A multiscale nonhydrostatic
950   atmospheric model using Centroidal Voronoi tessellations and C-grid staggering, Mon. Weather Rev., 140, 3090-
951   3105, https://doi.org/10.1175/MWR-D-11-00215.1, 2012.

952   Skamarock, W.C., and Coauthors: A description of the Advanced Research WRF version 3, NCAR Tech. Note
953   NCAR/TN-475+STR, 113 pp, 2008.

954   Smagorinsky, J.: General circulation experiments with the primitive equations. I. The basic experiment, Mon. Weather
955   Rev., 91, 99-164, https://doi.org/10.1175/1520-0493(1963)091<0099:GCEWTP>2.3.CO;2, 1963.

956 Stanfield, R.E., Dong, X., Xi, B., Del Genio, A.D., Minnis, P., Doelling, D., and Loeb, N.: Assessment of NASA
957   GISS CMIP5 and Post-CMIP5 simulated clouds and TOA radiation budgets using satellite observations. Part II:
958   TOA radiation budget and CREs, J. Climate, 28, 1842-1863, https://doi.org/10.1175/JCLI-D-14-00249.1, 2015.

959 Stephens, G.L., and Kummerow, C.D.: The remote sensing of clouds and precipitation from space: A review, J. Atmos.
960   Sci., 64, 3742-3765, https://doi.org/10.1175/2006JAS2375.1, 2007.

961 Stephens, G.L., Vane, D.G., Boain, R.J., Mace, G.G., Sassen, K., Wang, Z., Illingworth, A.J., O'Connor, E.J., Rossow,
962   W.B., Durden, S.L., Miller, S.D., Austin, R.T., Benedetti, A., Mitrescu, C., and the CloudSat Science Team: The
963   CloudSat mission and the A-Train: A new dimension and space-based observations of clouds and precipitation,
964   B. Am. Meteorol. Soc., 83, 1771-1790, https://doi.org/10.1175/BAMS-83-12-1771, 2002.

965 Storer, R.L., Griffin, B.M., Hoft, J., Weber, J.K., Raut, E., Larson, V.E., Wang, M., and Rasch, P.J.: Parameterizing
966   deep convection using the assumed probability density function method, Geosci. Model Dev., 8, 1-19,
967   https://doi.org/10.5194/gmd-8-1-2015, 2015.

968 Suhas, E., and Zhang, Q.J.: Evaluation of trigger functions for convective parameterization schemes using
969   observations, J. Climate, 27, 7647-7666, https://doi.org/10.1175/JCLI-D-13-00718.1, 2014.

970 Taylor, K.E., Stouffer, R.J., and Meehl, G.A.: An overview of CMIP5 and the experiment design, B. Am. Meteorol.
971   Soc., 93, 485-4398, https://doi.org/10.1175/BAMS-D-11-00094.1, 2012.

972 Thayer-Calder, K., Gettelman, A., Craig, C., Goldhaber, S., Bogenschutz, P.A., Chen, C.-C., Morrison, H., Höft, J.,
973   Raut, E., Griffin, B.M., Weber, J.K., Larson, V.E., Wyant, M.C., M. Wang, Guo, Z., and Ghan, S.J.: A unified
974   parameterization of clouds and turbulence using CLUBB and subcolumns in the Community Atmosphere Model,
975   Geosic. Model Dev., 8, 3801-3821, https://doi.org/10.5194/gmd-8-3801-2015, 2015.

976 Thompson, G., Field, P.R., Rasmussen, R.M., and Hall, W.D.: Explicit forecasts of winter precipitation using an
977   improved bulk cloud microphysics scheme. Part II: Implementation of a new snow parameterization, Mon.
978   Weather Rev., 136, 5095-5115, https://doi.org/10.1175/2008MWR2387.1, 2008.

979 Thompson, G., Rasmussen, R.M. , and Manning, K.: Explicit forecasts of winter precipitation using an improved bulk
980   cloud microphysics scheme. Part I: Description and sensitivity analysis, Mon. Weather Rev., 132, 519-542,
981   https://doi.org/10.1175/1520-0493(2004)132<0519:EFOWPU>2.0.CO:2, 2004.

982 Thompson, G., Tewari, M., Ikeda, K., Tessendorf, S., Weeks, C., Otkin, J., and Kong, F.: Explicitly-coupled cloud
983   physics and radiation parameterizations and subsequent evaluation in WRF high-resolution convective forecasts,
984   Atmos. Res., 168, 92-104, https://doi.org/10.1016/j.atmosres.2015.09.005, 2016.

985 Tokioka, T., Yamazaki, K., Kotoh, A., and Ose, T.: The equatorial 30-60 day oscillation and the Arakawa–Schubert
986   penetrative   cumulus   parameterization,   J.   Meteor.   Soc.   Japan,   66,   883–900,
987   https://doi.org/10.2151/jmsj1965.66.6_883, 1988.

988 Waliser, D.E., Li, J.-L., Woods, C.P., Austin, R.T., Bacmeister, J., Chern, J., Del Genio, A., Jiang, J.H., Juang, Z.,
989   Meng, H., Minnis, P., Platnick, S., Rossow, W.B., Stephens, G.L., Sun-Mack, S., Tao, W.-K., Tompkins, A.M.,

990   Vane, D.G., Walker, C., and Wu, D.: Cloud ice: A climate model challenge with signs and expectations of
991   progress, J. Geophys. Res., 114, D00A21, https://doi.org/10.1029/2008JD010015, 2009.

992   Wicker, L.J., and W.C. Skamarock: Time-splitting methods for elastic models using forward time schemes, Mon.
993   Weather Rev., 130, 2088-2097, https://doi.org/10.1175/1520-0493(2002)130<2088:TSMFEM>2.0.CO;2, 2002.

994   Wielicki, B.A., Barkstrom, B.R., Harrison, E.F., Lee III, R.B., Smith, G.L., and Cooper, J.E.: Clouds and the Earth's
995   Radiation Energy System (CERES): An Earth Observing System experiment, B. Am. Meteorol. Soc., 77, 853-
996   868, https://doi.org/10.1175/1520-0477(1996)077<0853:CATERE>2.0.CO;2, 1996.

997   Wong, M., and Skamarock, W.C.: Spectral characteristics of convective-scale precipitation observations and forecasts,
998   Mon. Weather Rev., 144, 4183-4195, https://doi.org/10.1175/MWR-D-16-0183.1, 2016.

999   Xu, K.-M. and Krueger, S.K.: Evaluation of cloudiness parameterizations using a cumulus ensemble model, Mon.
1000   Weather Rev., 119, 342-367, https://doi.org/10.1175/1520-0493(1991)119<0342:EOCPUA>2.0.CO;2, 1991.

1001   Xu, K.-M., and Randall, D. A.: A semi-empirical cloudiness parameterization for use in climate models, J. Atmos.
1002   Sci., 53, 3084–3102, https://doi.org/10.1175/1520-0469(1996)053<3084:ASCPFU>2.0.CO;2, 1996.

1003   Zheng, Y., Alapaty, K., Herwehe, J. A., Del Genio, A.D., and Niyogi, D.: Improving high-resolution weather forecasts
1004   using the Weather Research and Forecasting (WRF) model with an updated Kain-Fritsch scheme, Mon. Weather
1005   Rev., 144, 833-860, https://doi.org/10.1175/MWR-D-15-0005.1, 2016.